A gradient enhanced constitutive framework for the investigation of ductile damage localization within semicrystalline polymers

Soheil Satouri, George Chatzigeorgiou, Adil Benaarbia, Fodil Meraghni

Article

INTERNATIONAL JOURNAL OF DAMAGE MECHANICS

International Journal of Damage Mechanics
0(0) 1–37

DOI: 10.1177/10567895221115459
journals.sagepub.com/home/ijd

SAGE

A gradient enhanced constitutive framework for the investigation of ductile damage localization within semicrystalline polymers

Soheil Satouri, George Chatzigeorgiou, Adil Benaarbia and Fodil Meraghni

Abstract

The paper presents a gradient enhanced model dealing with nonlocal phenomena driven by the ductile damage in semicrystalline polymers that exhibit rate-dependent and rate-independent mechanisms. The study aims at capturing the material localization at high damage levels. To this end, a viscoelastic-viscoplastic constitutive model is formulated considering a gradient enhanced thermodynamic potential, function of local and nonlocal state variables. The model is based on two different options for the nonlocal state variable: the first option considers nonlocal damage scalar, while the second considers nonlocal hardening state variable. An appropriate user defined material subroutine is developed so as to define and to update the stress, the state variables, and the associated tangent moduli towards finite element structural computations. The analogy between the steady-state heat equation and the nonlocal gradient enhanced relation enables coupling the displacement and nonlocal fields within a finite element package code (i.e., ABAQUS). Structural analyses for polyamide 66 (PA66) material are presented to assess the efficiency of the developed nonlocal model. This research work demonstrates that the model is able to capture efficiently the ductile damage localization and simulate the related fields when using the nonlocal hardening or damage state variable. This study for the first time combines viscoelasticity, viscoplasticity, and damage with nonlocal approaches, and can be considered as an initial step towards developing a constitutive formulation towards multiscale analyses for polymer-based composites.

Keywords

Thermodynamics, viscoplasticity, nonlocal modeling, gradient enhanced potential, semicrystalline polymers

Arts et Métiers Institute of Technology, CNRS, Université de Lorraine, LEM3, Metz, France

Corresponding author:
Fodil Meraghni, Arts et Métiers Institute of Technology, CNRS, Université de Lorraine, LEM3, F-57000, Metz, France.
Email: fodil.meraghni@ensam.eu

Introduction

Polymeric materials are very popular thanks to their high performance and ease of use in a variety of industries such as automotive, aerospace, packaging, and medical equipment. In this regard, researchers have presented many constitutive models in the literature so as to describe the complex deformation mechanisms (Arif et al., 2014; Arruda and Boyce, 1993; Boyce et al., 1988; Breemen et al., 2011; Buckley and Jones, 1995; Govaert et al., 2000; Klompen et al., 2005; Nouri et al., 2009; Praud et al., 2021; Tervoort et al., 1998). Polymers often exhibit softening and consequently material instability after exceeding a certain level of plastic deformation, for which the conventional continuum models are not capable of characterizing the material behavior within the highly damaged zones. As a matter of fact, the tendency for releasing the least amount of inelastic stored energy during the failure leads to internal variables localization into narrowest areas (Benaarbia et al., 2014; Pamin, 1994), leading to non-objective solutions when refining the mesh in the computational models. To address this issue, the local model is often modified using the nonlocal framework as a form of "localization limiters", in which the length scale is included so as to derive objective responses (Bažant, 1976; Bazant and Lin, 1988).

In this respect, different nonlocal approaches are reported in the open literature. Some authors apply the integral form in which the local variable is replaced by its nonlocal counterpart derived by a weighted average over the corresponding neighborhood (Jirásek, 1998, 2002, 2007; Jirásek et al., 2004; Pijaudier-Cabot and Bažant, 1987). In this manner, nonlocal variables depend not only on their local positions but also on their weighted average in the whole body. The Taylor expansion of the integral nonlocal formulation yields to gradient enhanced forms that are more simple to implement into finite element codes compared to the integral one, and the interaction between local and nonlocal variables are defined through their gradients (Bažant et al., 1984; Dimitrijevic and Hackl, 2011; Forest, 2009; Jirásek, 2007; Peerlings et al., 2001). In addition, other methods based on phase field, micromorphic, and peridynamics approaches are also widely employed in the literature, for which more detailed information is available in (Borst and Verhoosel, 2016; Miehe et al., 2010, 2016; Saanouni and Hamed, 2013; Silling, 2000; Silling and Lehoucq, 2010). In reference to what is mentioned above, there are two types of nonlocal gradient models: explicit and implicit forms. The first one is derived through the Taylor expansion of the nonlocal integral formulation (Al-Rub and Voyiadjis, 2004; Engelen et al., 2003). The second one is another simplification of the integral form, deduced from the explicit one, for which solutions are often in a good agreement with the classical integral type (Borst et al., 1998; Peerlings et al., 2001; Seupel et al., 2018).

Regarding the choice of the nonlocal variable, many approaches in the open literature consider plastic deformation, equivalent strain, damage, etc. as nonlocal variables (Brepols et al., 2017; Geers et al., 1999; Pijaudier-Cabot and Bažant, 1987; Simone et al., 2004; Wu et al., 2013). In this connection, Saanouni and Hamed presented a nonlocal micromorphic model based on various nonlocal variables and used the micromorphic damage variable to characterize the material behavior in the softening phase (Saanouni and Hamed, 2013). To ensure a proper connection between local and nonlocal variables, several options can be adopted. Indeed, the chosen local variable can be either enforced to behave as its nonlocal counterpart through Kuhn-Tucker conditions (Seupel et al., 2018) or directly replaced by the nonlocal variable in the constitutive laws (Geers et al., 2000). As an efficient alternative, one can propose a thermodynamically based extended framework, in which the free energy is enhanced with a nonlocal term including the nonlocal variable and its gradient (Dimitrijevic and Hackl, 2011; Forest, 2009; Kiefer et al., 2018; Ostwald et al., 2019).

This study proposes a nonlocal thermodynamically based framework for semicrystalline polyamides formulated under small deformation and rotation assumption. It performs a parametric study to investigate the capability of the gradient enhanced model in yielding mesh objective and physically meaningful solutions within the highly damaged zones under softening, which considers the nonlinear rheology of the material including all inelastic mechanisms (viz. viscoelasticity at different time scales, VE, viscoplasticity, VP, ductile damage, D, etc.). It also introduces the nonlocal hardening state variable to address the damage localization in a VEVPD model, where its efficiency is justified compared to the nonlocal damage. Since the framework is developed for polyamide materials, the goal is to adopt the model in multiscale analyses. For fiber-reinforced composites, the deformation levels are usually small, thus it is reasonable to develop the present nonlocal framework using small deformations/rotations hypothesis.

This paper is organized as follows: in the next section, the constitutive laws of the considered material are derived for both nonlocal damage and nonlocal hardening state variable. In section 'Numerical implementation', the return mapping numerical approach as well as the nonlocal model implementation are established. In section 'Numerical examples and discussions', a parametric analysis is provided to explore the ductile damage development and mesh objectivity of the nonlocal model based on benchmark examples.

In this study, the tensor notations are explained as follows: the bold and blackboard symbols represent the second and fourth order tensors, respectively, and the others denote the scalar variables. In addition, the following tensor products are used in this work:

$$\boldsymbol{P} : \boldsymbol{Q} = P_{ij} : Q_{kl}, \quad (\mathbb{P} : \boldsymbol{Q})_{ij} = P_{ijkl} Q_{kl}, \quad (\boldsymbol{P} \otimes \boldsymbol{Q})_{ijkl} = \boldsymbol{P}_{ij} \boldsymbol{Q}_{kl}$$

Gradient enhanced constitutive modelling

Nonlinear behavior of polyamides

Based on the open literature (Arif et al., 2014; Benaarbia et al., 2014, 2014, 2016, 2019; Praud et al., 2017), semicrystalline polyamides exhibit highly nonlinear and dissipative mechanisms including viscoelasticity at different time scales, viscoplasticity, and ductile damage. Many constitutive laws have then been proposed to capture this nonlinear behavior using physics-based (Arruda and Boyce, 1993; Billon, 2012) and phenomenological approaches (Benaarbia et al., 2018; Krairi and Doghri, 2014; Launay et al., 2011; Praud et al., 2017). Most of these models have been formulated within the framework of Thermodynamics of Irreversible Processes, TIP, (Germain et al., 1983; Halphen and Nguyen, 1975). For the polyamide 66, cyclic creep recovery tests have been conducted in (Benaarbia et al., 2014, 2016) and have shown that capturing the material behavior requires to assume that the total strain can be decomposed into decoupled viscoelastic and viscoplastic strain components (Gudimetla and Doghri, 2017). In the present study, a viscoelastic viscoplastic (VEVP) rheological model is adopted to describe the dissipative mechanisms during the deformation process of the material.

To account for the viscoelasticity, several models have been proposed in the literature (Chen et al., 2012; Papanicolaou and Zaoutsos, 2011; Rodas et al., 2014; Simo and Hughes, 2006), among which the Kelvin-Voight is applied in this work, whereas the viscoplastic mechanisms can be captured based on either unified or non-unified viscoplasticity theories (Chaboche, 2008). Hereafter,

the viscoplastic behavior is modelled based on the unified theory considering an isotropic hardening function. The reduction in the material stiffness is taken into account by introducing a damage internal variable, D, based on the effective stress concept (Chaboche, 1997; Kachanov, 1958; Rabotnov, 1968).

The linear viscoelastic response of the material model is accounted for through a certain number N_v of Kelvin-Voigt branches, in which a linear spring is connected to a dashpot in parallel. Defining more than one Kelvin-Voigt branch allows capturing creep and relaxation for several characteristic times (Praud et al., 2017). The viscoplastic mechanism is modelled by considering a parallel assembly of a nonlinear spring, a nonlinear dashpot, and a friction rheological element with an initial yield stress, R_o. The latter is activated once the model exceeds the von-Mises plastic yield surface, f:

$$f(\boldsymbol{\sigma}, -R;\ \ D, r) = \frac{\sigma^{eq}(\boldsymbol{\sigma})}{1-D} - R(r) - R_0 \tag{1}$$

where $\boldsymbol{\sigma}$, R, and r denote the second order stress tensor, the conjugate, and state variables of the isotropic hardening, respectively. The term σ^{eq} stands for the equivalent stress defined as $\sigma^{eq} = \sqrt{\frac{3}{2}\boldsymbol{\sigma}' : \boldsymbol{\sigma}'}$, where $\boldsymbol{\sigma}'$ is the deviatoric part of the stress tensor while the symbol "$:$" defines the double contracted product. The hardening state variable rate $\dot{r}$ is considered as follows:

$$\dot{r} = \left\langle \frac{f(\boldsymbol{\sigma}, -R;\ \ D, r)}{R_{vp}} \right\rangle_{+}^{p_{vp}^{-1}} \tag{2}$$

where "$\langle\rangle_+$" denotes the Macaulay brackets, and R_{vp} and p_{vp} are respectively, the viscoplastic resistance and exponent. Here, D denotes the scalar ductile damage variable driven by plasticity, whose evolution directly depends on the hardening state variable rate, $\dot{r}$, as:

$$\dot{D} = \Lambda_D \, \dot{r} \tag{3}$$

which is derived through the evolution laws and discussed at section 'State and evolution laws'.

Detailed exposition of the local model constitutive relations and evolution laws is given in (Praud et al., 2017). Considering the above inelastic mechanisms, the Euler-Lagrange equations for the nonlocal framework based on the thermodynamic principles are derived as in the following section.

Thermodynamically based Euler-Lagrange equations

In this section, a thermodynamically based nonlocal model is presented to capture the size effect at the microscale and to address the loss of uniqueness on the local model response during the material softening. To this end, an internal state variable, φ, its nonlocal counterpart, φ^{nl}, and its gradient, $\boldsymbol{\nabla}_{\boldsymbol{x}}\varphi^{nl}$, are introduced into the thermodynamic potential to describe the nonlocal phenomena within isothermal conditions (Dimitrijevic and Hackl, 2011; Forest, 2009):

$$\Psi\left(\boldsymbol{\epsilon}, \{\boldsymbol{\chi}_i\}_{i=2,N}, \varphi, \varphi^{nl}, \boldsymbol{\nabla}_{\boldsymbol{x}}\varphi^{nl}\right) = \Psi^{l}\left(\boldsymbol{\epsilon}, \{\boldsymbol{\chi}_i\}_{i=2,N}, \varphi\right) + \Psi^{nl}\left(\varphi, \varphi^{nl}, \boldsymbol{\nabla}_{\boldsymbol{x}}\varphi^{nl}\right) \tag{4}$$

where $\boldsymbol{\epsilon}$ denotes the total strain tensor, and $\{\boldsymbol{\chi}_i\}_{i=2,N}$ is the set of internal state variables which can be scalar or tensorial. Therein, the thermodynamic state of the polyamide is described through the following internal variables:

- the state variable, φ, defined as follows:

$$\varphi = \chi_1 = r, \;\; D = \chi_2, \;\; \text{or} \;\; \varphi = \chi_1 = D, \quad r = \chi_2$$

- the viscoplastic deformation, $\boldsymbol{\epsilon}^{vp} = \boldsymbol{\chi}_3$,
- and the elementary viscoelastic strain components, $\{\boldsymbol{\epsilon}^{vi}\}_{i=1,N_v} = \{\boldsymbol{\chi}_i\}_{i=4,N_v+3}$, of Kelvin-Voight branches.

The local potential Ψ^l is split into an elastic part, Ψ^e, a set of viscoelastic potentials, $\{\Psi^{vi}\}_{i=1,N_v}$, and finally the viscoplastic free energy, Ψ^{vp}:

$$\Psi^l\left(\boldsymbol{\epsilon}, \boldsymbol{\epsilon}^{vp}, \{\boldsymbol{\epsilon}^{vi}\}_{i=1,N_v}, r, D\right) = \Psi^e\left(\boldsymbol{\epsilon}, \boldsymbol{\epsilon}^{vp}, \{\boldsymbol{\epsilon}^{vi}\}_{i=1,N_v}, D\right) + \sum_{i=1}^{N^v} \Psi^{vi}\left(\boldsymbol{\epsilon}^{vi}, D\right) + \Psi^{vp}(r) \tag{5}$$

with

$$\Psi^e = \frac{1}{2}\left(\boldsymbol{\epsilon} - \sum_{i=1}^{N_v} \boldsymbol{\epsilon}^{vi} - \boldsymbol{\epsilon}^{vp}\right) : (1-D)\mathbb{C}^e : \left(\boldsymbol{\epsilon} - \sum_{i=1}^{N_v} \boldsymbol{\epsilon}^{vi} - \boldsymbol{\epsilon}^{vp}\right) \tag{6a}$$

$$\Psi^{vi} = \frac{1}{2}\boldsymbol{\epsilon}^{vi} : (1-D)\mathbb{C}^{vi} : \boldsymbol{\epsilon}^{vi}, \;\; \text{for i} = 1, \ldots, N_v \tag{6b}$$

$$\Psi^{vp} = \int_0^r R(r)\mathrm{d}r \tag{6c}$$

The nonlocal thermodynamic potential Ψ^{nl} is expressed as (Forest, 2009):

$$\Psi^{nl}\left(\varphi, \varphi^{nl}, \boldsymbol{\nabla}_{\boldsymbol{x}}\varphi^{nl}\right) = \frac{\xi^{nl}}{2}\|\boldsymbol{\nabla}_{\boldsymbol{x}}\varphi^{nl}\|^2 + \frac{1}{2}\gamma^{nl}\left(\varphi - \varphi^{nl}\right)^2 \tag{7}$$

where the operator "$||\,.\,||$" denotes the second norm, while ξ^{nl} and γ^{nl} stand for the nonlocal model parameters considered positive. They introduce the length scale effect into the thermodynamic potential as $l^{nl} = \sqrt{\xi^{nl}/\gamma^{nl}}$. The gradient parameter ξ^{nl} determines the degree of regularization governing the nonlocal part of the free energy and is derived from the internal length scale incorporating the microstructural effects into the model (Dimitrijevic and Hackl, 2011; Kiefer et al., 2018; Ostwald et al., 2019). The nonlocal parameter γ^{nl} is assigned to ensure that i) the local variable behaves as closely as possible to its nonlocal counterpart, and ii) the performed analyses are mesh objective.

Considering the above thermodynamic potential, the equilibrium equations are obtained using the minimum potential energy postulate. Accordingly, the total potential energy, PE, in a reference domain $\mathcal{B}$ is the sum of external, $-PE_{ext}$, and internal, PE_{int}, potential energies:

$$PE = PE_{int} - PE_{ext} = \int_{\mathcal{B}} \Psi\left(\boldsymbol{\epsilon}, \{\boldsymbol{\chi}_i\}_{2=1,N}, \varphi, \varphi^{nl}, \boldsymbol{\nabla}_{\boldsymbol{x}}\varphi^{nl}\right) \mathrm{d}V - \int_{\mathcal{B}} \boldsymbol{u}.\boldsymbol{F}_b \, \mathrm{d}V - \int_{\partial\mathcal{B}} \boldsymbol{u}.\boldsymbol{F}_s \, \mathrm{d}S \tag{8}$$

where $\boldsymbol{F}_b$ and $\boldsymbol{F}_s$ are respectively the external force per unit volume and external force per unit surface, and $\boldsymbol{u}$ denotes the associated displacement field.

The minimum potential energy postulate allows to write:

$$\{\boldsymbol{u}, \varphi^{nl}\} = arg[\min_{\boldsymbol{u},\varphi^{nl}\in\mathcal{B}}(PE)] \tag{9}$$

Accordingly, the differential of the potential energy with respect to the displacement field, $\boldsymbol{u}$, and the nonlocal variable, φ^{nl}, is set to zero:

$$\frac{\partial PE}{\partial \boldsymbol{u}}.\delta\boldsymbol{u} = \int_{\mathcal{B}} \frac{\partial \Psi}{\partial \boldsymbol{\epsilon}} : \left(\frac{\partial \boldsymbol{\epsilon}}{\partial \boldsymbol{u}}.\delta\boldsymbol{u}\right) \mathrm{d}V - \int_{\mathcal{B}} \boldsymbol{F}_b.\delta\boldsymbol{u} \, \mathrm{d}V - \int_{\partial\mathcal{B}} \boldsymbol{F}_s.\delta\boldsymbol{u} \, \mathrm{d}S = 0 \tag{10a}$$

$$\frac{\partial PE}{\partial \varphi^{nl}}\delta\varphi^{nl} = \int_{\mathcal{B}} \left[\xi^{nl}\boldsymbol{\nabla}_{\boldsymbol{x}}\varphi^{nl}.\boldsymbol{\nabla}_{\boldsymbol{x}}\delta\varphi^{nl} - \gamma^{nl}\left(\varphi - \varphi^{nl}\right)\delta\varphi^{nl}\right] \mathrm{d}V = 0 \tag{10b}$$

Based on the small deformations assumption, the strain tensor can be replaced by the symmetrical gradient of the displacement field $\boldsymbol{\nabla}_{\boldsymbol{x}}^{sym}\boldsymbol{u}$. Substituting it into equation (10a) and using the Gauss-Ostrogradski theorem results in:

$$-\int_{\mathcal{B}} (\boldsymbol{\nabla}_{\boldsymbol{x}}.\boldsymbol{\sigma}).\delta\boldsymbol{u} \, \mathrm{d}V + \int_{\partial\mathcal{B}} (\boldsymbol{\sigma}.\boldsymbol{n}).\delta\boldsymbol{u} \, \mathrm{d}S - \int_{\mathcal{B}} \boldsymbol{F}_b.\delta\boldsymbol{u} \mathrm{d}V - \int_{\partial\mathcal{B}} \boldsymbol{F}_s.\delta\boldsymbol{u} \, \mathrm{d}S = 0 \tag{11}$$

Using Gauss-Ostrogradski theorem, equation (10b) is expanded as:

$$\int_{\partial\mathcal{B}} \xi^{nl}\boldsymbol{\nabla}_{\boldsymbol{x}}\varphi^{nl}\delta\varphi^{nl}.\boldsymbol{n} \, \mathrm{d}S - \int_{\mathcal{B}} \xi^{nl} \, \boldsymbol{\nabla}_{\boldsymbol{x}}^2\varphi^{nl}\delta\varphi^{nl} \, \mathrm{d}V - \int_{\mathcal{B}} \gamma^{nl}\left(\varphi - \varphi^{nl}\right)\delta\varphi^{nl} \, \mathrm{d}V = 0 \tag{12}$$

From equations (11) and (12), the Euler-Lagrange equations with the associated boundary conditions are derived:

- Stress equilibrium:

$$\boldsymbol{\nabla}_{\boldsymbol{x}}. \, \boldsymbol{\sigma} + \boldsymbol{F}_b = 0 \quad \forall \boldsymbol{x} \in \mathcal{B}, \quad \boldsymbol{\sigma}.\boldsymbol{n} - \boldsymbol{F}_s = 0 \quad \forall \boldsymbol{x} \in \partial\mathcal{B} \tag{13}$$

- Nonlocal balance equation:

$$\xi^{nl}\boldsymbol{\nabla}_{\boldsymbol{x}}^2\varphi^{nl} + \gamma^{nl}\left(\varphi - \varphi^{nl}\right) = 0 \quad \forall \boldsymbol{x} \in \mathcal{B}, \quad \boldsymbol{\nabla}_{\boldsymbol{x}}\varphi^{nl}.\boldsymbol{n} = 0 \quad \forall \boldsymbol{x} \in \partial\mathcal{B} \tag{14}$$

State and evolution laws

The conjugate state variables, $\{A_i\}_{i=1,N}$ can be derived from the partial derivative of the thermodynamic potential with respect to the internal state variables, $\{\chi_i\}_{i=1,N}$, as follows (see Table 1):

$$A_i = \frac{\partial \Psi}{\partial \boldsymbol{\chi}_i}, \text{ with } i = 1, \ldots, N \tag{15}$$

Aside this, the partial derivatives of the nonlocal term, Ψ^{nl}, lead to the following nonlocal conjugate state variables:

$$Y_{\varphi^{nl}} = \frac{\partial \Psi}{\partial \varphi^{nl}}, \quad \boldsymbol{Y}_{\nabla_{\boldsymbol{x}}\varphi^{nl}} = \frac{\partial \Psi}{\partial \nabla_{\boldsymbol{x}}\varphi^{nl}} \tag{16}$$

Accordingly, using the rate form of the free energy, the intrinsic mechanical dissipation inequality is expressed by:

$$\mathcal{D} = P_m - \dot{\Psi} \geq 0 \tag{17}$$

where P_m is the sum of strain and nonlocal energy rates such that:

$$P_m = \boldsymbol{\sigma} : \dot{\boldsymbol{\epsilon}} + Y_{\varphi^{nl}} \dot{\varphi^{nl}} + Y_{\nabla_{\boldsymbol{x}}\varphi^{nl}} \cdot (\nabla_{\boldsymbol{x}} \dot{\varphi^{nl}}) \tag{18}$$

According to the state laws (see Table 1) and substituting into equation (17), the dissipation is expanded to:

$$\mathcal{D} = \boldsymbol{\sigma} : \dot{\boldsymbol{\epsilon}} + Y_{\varphi^{nl}} \dot{\varphi^{nl}} + Y_{\nabla_{\boldsymbol{x}}\varphi^{nl}} \cdot (\nabla_{\boldsymbol{x}} \dot{\varphi^{nl}}) - \left(\frac{\partial \Psi}{\partial \boldsymbol{\epsilon}} : \dot{\boldsymbol{\epsilon}} + \sum_{i=1}^{N} \frac{\partial \Psi}{\partial \chi_i} : \dot{\chi}_i + \frac{\partial \Psi}{\partial \varphi^{nl}} \dot{\varphi^{nl}} + \frac{\partial \Psi}{\partial \nabla_{\boldsymbol{x}}\varphi^{nl}} \cdot (\nabla_{\boldsymbol{x}} \dot{\varphi^{nl}}) \right) \tag{19}$$

Table 1. State and evolution laws for the local model (Lemaitre and Chaboche, 1990) enhanced by the nonlocal and gradient components ($\dot{\lambda}$ stands for the viscoplastic multiplier and both $\boldsymbol{\Lambda}_{vp}$ and Λ_D are the viscoplastic and damage directions, respectively).

State variables	Conjugate (dual) variables	Evolution laws
Observable		
Strain tensor, $\boldsymbol{\epsilon}$	$\boldsymbol{\sigma} = \frac{\partial \Psi}{\partial \boldsymbol{\epsilon}}$	–
Internal		
Viscoelastic strains, $\boldsymbol{\epsilon}^{ve}$	$-\boldsymbol{\sigma}^{ve} = \frac{\partial \Psi}{\partial \boldsymbol{\epsilon}^{ve}} = (1 - D)\mathbb{C}^{ve} : \boldsymbol{\epsilon}^{ve} - \boldsymbol{\sigma}$	$\dot{\boldsymbol{\epsilon}}^{ve} = \frac{\partial \Omega^{ve}}{\partial \boldsymbol{\sigma}^{ve}} = \frac{(\mathbb{V}^{ve})^{-1}}{(1-D)} : \boldsymbol{\sigma}^{ve}$
Viscoplastic strain, $\boldsymbol{\epsilon}^{vp}$	$-\boldsymbol{\sigma} = \frac{\partial \Psi}{\partial \boldsymbol{\epsilon}^{vp}}$	$\dot{\boldsymbol{\epsilon}}^{vp} = \frac{\partial F}{\partial \boldsymbol{\sigma}} \dot{\lambda} = \boldsymbol{\Lambda}_{vp} \dot{\lambda}$
Hardening state variable, r	$R = \frac{\partial \Psi}{\partial r}$	$\dot{r} = -\frac{\partial F}{\partial R} \dot{\lambda} = \dot{\lambda}$
Damage variable, D	$-Y = \frac{\partial \Psi}{\partial D}$	$\dot{D} = \frac{\partial F}{\partial Y} \dot{\lambda} = \left(\frac{Y}{S_D} \right)^{\beta_D} \frac{\dot{\lambda}}{1-D} = \Lambda_D \dot{\lambda}$

From equation (16), the nonlocal terms can be canceled out, and the dissipation is expressed as:

$$\mathcal{D} = \sum_{i=1}^{N_v} \boldsymbol{\sigma}^{vi} : \dot{\boldsymbol{\epsilon}}^{vi} + \boldsymbol{\sigma} : \dot{\boldsymbol{\epsilon}}^{vp} - R\dot{r} + Y\dot{D} \geq 0, \text{ with } -Y = \frac{\partial \Psi}{\partial D} \tag{20}$$

According to the Generalized Standard Materials formalism, GSM, the evolution laws presented in Table 1 are derived through convex dual dissipation and indicative functions (Halphen and Nguyen, 1975). A set of sub-potentials, Ω^{vi}, are introduced to derive the elementary viscoelastic strain rates, $\dot{\boldsymbol{\epsilon}}^{vi}$, with respect to their associated thermodynamic forces, $\boldsymbol{\sigma}^{vi}$, such that:

$$\Omega^{vi}\left(\boldsymbol{\sigma}^{vi}, D\right) = \frac{1}{2}\boldsymbol{\sigma}^{vi} : \frac{\mathbb{V}^{vi-1}}{(1-D)} : \boldsymbol{\sigma}^{vi} \tag{21}$$

where $\mathbb{V}^{vi}$ denotes the viscosity tensor of the ith viscoelastic Kelvin-Voigt branch. According to the J_2-viscoplasticity theory (Simo and Hughes, 2006), the viscoplastic evolution laws coupled with damage are derived using the normality rule by considering the following indicative function, F:

$$F = f(\boldsymbol{\sigma}, -R;\ D, r) + f_D(Y, D) \text{ with } f_D = \frac{S_D}{(\beta_D + 1)(1-D)}\left(\frac{Y}{S_D}\right)^{\beta_D+1} \tag{22}$$

where β_D and S_D are damage related parameters. Table 1 gives a summary of the evolution laws used in the current model.

In order to capture the damage localization and to address the mesh sensitivity during FE computations, the nonlocal model is formulated based on two different nonlocal variable cases: the first considers the nonlocal damage, D^{nl}, as the nonlocal variable by enhancing the damage release energy, Y, while the second considers the nonlocal hardening state variable, r^{nl}, by modifying the hardening function, R. The constitutive laws related to both cases are derived in the following sections.

Case 1: Nonlocal damage variable

Replacing φ^{nl} by D^{nl} in equation (7), the nonlocal free energy can be re-expressed as:

$$\Psi^{nl}\left(D, D^{nl}, \boldsymbol{\nabla}_{\boldsymbol{x}} D^{nl}\right) = \frac{\xi^{nl}}{2}||\boldsymbol{\nabla}_{\boldsymbol{x}} D^{nl}||^2 + \frac{1}{2}\gamma^{nl}(D - D^{nl})^2 \tag{23}$$

According to the state laws, the damage release energy, Y, can be decomposed as:

$$-Y = \frac{\partial \Psi}{\partial D} = -Y^{l} - Y^{nl}, \text{ with } -Y^{l} = \frac{\partial \Psi^{l}}{\partial D} \text{ and } -Y^{nl} = \frac{\partial \Psi^{nl}}{\partial D} \tag{24}$$

where the local part, Y^l, is obtained as:

$$Y^{l} = \frac{1}{2}\left(\boldsymbol{\epsilon} - \sum_{i=1}^{N_v} \boldsymbol{\epsilon}^{vi} - \boldsymbol{\epsilon}^{vp}\right) : \mathbb{C}^{e} : \left(\boldsymbol{\epsilon} - \sum_{i=1}^{N_v} \boldsymbol{\epsilon}^{vi} - \boldsymbol{\epsilon}^{vp}\right) + \frac{1}{2}\sum_{i=1}^{N_v} \boldsymbol{\epsilon}^{vi} : \mathbb{C}^{vi} : \boldsymbol{\epsilon}^{vi} \tag{25}$$

The nonlocal term, Y^{nl}, is given by:

$$Y^{nl} = -\gamma^{nl}(D - D^{nl}) \tag{26}$$

Y^{nl} is often a negative value added to the positive Y^{l} (Dimitrijevic and Hackl, 2008). In certain instances, the total Y becomes negative and violates the positivity of the dissipation. This can be prevented through considering only the positive part of Y in the damage related indicative function, f_D, as follows:

$$f_D = \frac{S_D}{(\beta_D + 1)(1 - D)} \left(\frac{\langle Y \rangle_+}{S_D} \right)^{\beta_D + 1} \tag{27}$$

Substituting equation (27) into the damage evolution law (see Table 1) yields:

$$\dot{D} = \left(\frac{1 + sgn(Y)}{2} \right) \left(\frac{\langle Y \rangle_+}{S_D} \right)^{\beta_D} \frac{\dot{\lambda}}{1 - D} \tag{28}$$

where "$sgn(.)$" denotes the sign function.

Case 2: nonlocal hardening state variable

In the second case, the nonlocal hardening state variable, r^{nl}, can be adopted to limit the damage localization within the softening zones. Thus, substituting the nonlocal hardening state variable, r^{nl}, into the thermodynamic potential, Ψ, in equation (7) leads to:

$$\Psi^{nl}\left(r, r^{nl}, \nabla_x r^{nl}\right) = \frac{\xi^{nl}}{2} ||\nabla_x r^{nl}||^2 + \frac{1}{2}\gamma^{nl}(r - r^{nl})^2 \tag{29}$$

It is worth mentioning that since the damage evolution is derived by the evolution of the hardening state variable, r, the nonlocal hardening state variable, r^{nl}, also affects the ductile damage implicitly. Substituting the above nonlocal energy equation (29) into equation (4), the hardening state function is enhanced with the nonlocal term, R^{nl}, as follows:

$$R(r) = \frac{\partial \Psi}{\partial r} = R^{l} + R^{nl} \tag{30}$$

with:

$$R^{l} = H_m r^{H_p}, \quad R^{nl} = \frac{\partial \Psi^{nl}}{\partial r} = \gamma(r - r^{nl}) \tag{31}$$

As indicated above, the constitutive laws are modified by introducing the nonlocal variables in two given cases and summarized in Table 2. Considering equations (30) and (31), if r^{nl} gets much larger than its local counterpart, r, then there is a possibility that the total hardening function becomes negative. However, as the next sections show, in all the analyses performed, this has not occurred.

Table 2. Modified associated variables in presence of the nonlocal variables along with the related evolution laws.

Nonlocal variable	Associated variables	Evolution laws
Nonlocal damage D^{nl}	$Y = Y^{l} + Y^{nl},\ Y^{nl} = -\gamma^{nl}(D - D^{nl})$	$\dot{D} = \frac{\partial F}{\partial Y}\dot{\lambda} = \left(\frac{Y}{S_D}\right)^{\beta_D}\frac{\dot{\lambda}}{1-D}$
	$Y_{\varphi^{nl}} = \frac{\partial \Psi}{\partial D^{nl}} = -\gamma^{nl}(D - D^{nl})$	$-$
	$\boldsymbol{Y}_{\nabla_x \varphi^{nl}} = \frac{\partial \Psi}{\partial \nabla_x D^{nl}} = \xi^{nl}\nabla_x D^{nl}$	$-$
	$R = R^{l}$	$\dot{r} = -\frac{\partial F}{\partial R}\dot{\lambda} = \dot{\lambda}$
Nonlocal hardening state variable r^{nl}	$Y = Y^{l}$	$\dot{D} = \frac{\partial F}{\partial Y}\dot{\lambda} = \left(\frac{Y}{S_D}\right)^{\beta_D}\frac{\dot{\lambda}}{1-D}$
	$Y_{\varphi^{nl}} = \frac{\partial \Psi}{\partial r^{nl}} = -\gamma^{nl}(r - r^{nl})$	$-$
	$\boldsymbol{Y}_{\nabla_x \varphi^{nl}} = \frac{\partial \Psi}{\partial \nabla_x r^{nl}} = \xi^{nl}\nabla_x r^{nl}$	$-$
	$R = R^{l} + R^{nl},\quad R^{nl} = \gamma^{nl}(r - r^{nl})$	$\dot{r} = -\frac{\partial F}{\partial R}\dot{\lambda} = \dot{\lambda}$

Numerical implementation

Gradient enhanced field development within the FE package code ABAQUS

The gradient model requires a nonlocal balance equation as well as the stress equilibrium. In order to impose the additional Euler-Lagrange equation into a commercial FE code like ABAQUS, several authors propose developing a user defined element (UEL) (Dimitrijevic and Hackl, 2011; Kiefer et al., 2018), in which, besides its inherent complexities, requires a considerable extent of programming. To avoid such technical problems, one can consider the nonlocal fields in a fully coupled temperature-displacement frame without developing a special UEL (Hortig, 2010; Ostwald et al., 2019). Assuming the steady state heat equation, the following analogy is derived:

$$K_c \nabla_{\boldsymbol{x}}{}^2\theta + h_g = 0 \iff \xi^{nl}\nabla_{\boldsymbol{x}}{}^2\varphi^{nl} + \gamma^{nl}\left(\varphi - \varphi^{nl}\right) = 0 \tag{32a}$$

$$\boldsymbol{q}.\boldsymbol{n} = 0 \iff \nabla_{\boldsymbol{x}}\varphi^{nl}.\boldsymbol{n} = 0 \tag{32b}$$

where K_c denotes the heat conduction, h_g the heat sources and $\boldsymbol{q}$ the heat flux vector derived from the Fourier's law:

$$\boldsymbol{q} = -K_c \nabla_{\boldsymbol{x}}\theta \tag{33}$$

Although, the thermomechanical tangent operators can be defined within the UMAT, it has never resulted in convergent solutions due to some unclear technical reasons (Seupel et al., 2018). Concerning this, HETVAL as an auxiliary user subroutine is employed to allow definition of the heat flux, heat sources, and interaction between internal state variables and the thermal field. In the present study, the HETVAL subroutine is adopted by replacing the temperature and its associated fields with the nonlocal scalar variable and the analogous fields.

Return mapping algorithm

The time discretization is implemented through a backward Euler scheme, based on which an arbitrary variable Ξ is updated from the time step n into the time step $n+1$ as $\Xi_{n+1} = \Xi_n + \Delta\Xi_{n+1}$. An iterative algorithm is required so as to solve the time discretized equations.

At the time step $n+1$ and the kth iteration, the iterative equations are expressed as $\Xi_{n+1}^{k+1} = \Xi_{n+1}^{k} + \delta\Xi_{n+1}^{k}$ and subsequently $\Delta\Xi_{n+1}^{k+1} = \Delta\Xi_{n+1}^{k} + \delta\Delta\Xi_{n+1}^{k}$. As a return mapping algorithm, convex cutting plane approach is employed to integrate the constitutive laws and update the state variables at each time step (Simo and Hughes, 2006; Qidwai and Lagoudas, 2000). To this end, the rate dependent constitutive relations are integrated through inelastic criteria whose nullity must be satisfied at each time step n:

$$\boldsymbol{\phi}^{vi} = \frac{1}{1-D}\left(\mathbb{V}^{vi}\right)^{-1} : \boldsymbol{\sigma}^{vi} - \dot{\boldsymbol{\epsilon}}^{vi} = 0, \quad \text{with } i = 1, \ldots, N_v \tag{34a}$$

$$\phi^{vp} = \dot{r} - \left\langle \frac{f(\boldsymbol{\sigma}, -R;\ D, r)}{R_{vp}} \right\rangle_{+}^{p_{vp}^{-1}} = 0 \tag{34b}$$

where $\boldsymbol{\sigma}^{vi}$ is given in Table 1, and $\boldsymbol{\phi}^{vi}$ and ϕ^{vp} are respectively the viscoelastic and viscoplastic criteria derived from the constitutive relations. Since the viscoelastic deformation is always activated, its associated criteria, $\boldsymbol{\phi}^{vi}$, have to be always satisfied. However, the viscoplastic criterion is taken into account once the viscoplastic deformation appears, where the equivalent effective stress exceeds the elastic limit, R_o, defined through the yield surface. Hence, the return mapping algorithm works in two steps: firstly, viscoelastic correction-prediction, and secondly, full correction.

Viscoelastic correction-prediction

As long as the plastic flow is not activated, the return mapping algorithm solely deals with the viscoelastic correction-prediction, in which only the elementary viscoelastic strains, $\boldsymbol{\epsilon}_{n+1}^{vi}$, at the time step $n+1$, evolves, and the rest of internal variables remain constant ($\delta r_{n+1} = \delta D_{n+1} = 0$ and $\delta\boldsymbol{\epsilon}_{n+1}^{vp} = 0$). The viscoelastic criteria converge to zero through the following iterative equation:

$$\boldsymbol{\phi}_{n+1}^{vi(k+1)} = \boldsymbol{\phi}_{n+1}^{vi(k)} + \delta\boldsymbol{\phi}_{n+1}^{vi(k)} = 0, \ \text{ with } i = 1, \ldots, N_v \tag{35}$$

For more simplicity, the subscription $n+1$ and superscriptions k are ignored in the following equations and the related expansions. Considering equation (34a), the viscoelastic criteria increments, $\delta\boldsymbol{\phi}^{vi}$, are properly determined with respect to $\delta\boldsymbol{\epsilon}^{vi}$ and substituted in equation (35):

$$\boldsymbol{\phi}^{vi} - \mathbb{A}^{vi} : \sum_{j=1(j\neq i)}^{N_v} \delta\boldsymbol{\epsilon}^{vj} \ - \mathbb{B}^{vi} : \delta\boldsymbol{\epsilon}^{vi} \ = 0, \ \text{ with } i = 1, \ldots, N_v \tag{36}$$

where the related mathematical procedure of deriving equation (36) is expressed in detail in Appendix 1. The expression (36) allows us to constitute a system of equations so as to update the viscoelastic criteria in each iteration as long as it converges to zero. Calculating $\boldsymbol{\epsilon}^{vi}$ and subsequently $\boldsymbol{\sigma}$ and σ^{eq}, the yield function sign, $sgn(f)$, determines whether the material is subjected to the plastic deformation or it still responds within the viscoelastic domain. In other words, the equivalent stress, σ^{eq}, smaller than the elastic limit, R_0, gives $f < 0$ which means there is no plastic flow where the algorithm goes to the next time step. On the contrary, when $f > 0$, the material has gone through

the viscoplastic deformation which requires full correction via enforcing both viscoelastic and viscoplastic criteria to be zero, as expressed in the following section.

Full correction

In the full correction step, the variation of all internal state variable increments ($\delta\boldsymbol{\epsilon}^{vi}_{n+1}$, $\delta\boldsymbol{\epsilon}^{vp}_{n+1}$, δr_{n+1}, and δD_{n+1}) are taken into account, while the nullity of viscoelastic and viscoplastic criteria must to be satisfied:

$$\begin{cases} \boldsymbol{\phi}^{vi(k+1)}_{n+1} = \boldsymbol{\phi}^{vi(k)}_{n+1} + \delta\boldsymbol{\phi}^{vi(k)}_{n+1} = 0, \ \text{with } i = 1, \ldots, N_v \ , \\ \phi^{vp(k+1)}_{n+1} = \phi^{vp(k)}_{n+1} + \delta\phi^{vp(k)}_{n+1} = 0 \end{cases} \tag{37}$$

Similarly, for more simplicity, k and $n+1$ are ignored for the following equations. Considering all internal variable increments, the viscoelastic and viscoplastic criteria increments (34) are expressed with respect to $\delta\boldsymbol{\epsilon}^{vi}$ and δr and substituted into equation (37):

$$\begin{cases} \mathbb{A}^{vi} : \displaystyle\sum_{j=1(j\neq i)}^{N_v} \delta\boldsymbol{\epsilon}^{vj} + \mathbb{B}^{vi} : \delta\boldsymbol{\epsilon}^{vi} + \boldsymbol{B}^{gi}\delta r = \boldsymbol{\phi}^{vi}, \\ \boldsymbol{A}^{vp} : \displaystyle\sum_{j=1}^{N_v} \delta\boldsymbol{\epsilon}^{vj} + B^{s}\delta r = \phi^{vp} \end{cases} \tag{38}$$

where the whole mathematical procedure of deriving equation (38) is expressed in detail within Appendix 1. The internal variable increments and subsequently the inelastic deformations, $\boldsymbol{\epsilon}^{vp}$ and $\boldsymbol{\epsilon}^{vi}$, are then derived allowing to update the stress tensor for the next time step.

Tangent operators

The UMAT subroutine, within the nonlocal framework, not only requires the tangent stiffness tensor $\mathbb{T}^{\boldsymbol{\sigma}}_{\boldsymbol{\epsilon}}$, but also the associated nonlocal tangent operators. Thus, considering the stress equilibrium, the stress increment $\Delta\boldsymbol{\sigma}$ is given by:

$$\Delta\boldsymbol{\sigma} = \mathbb{T}^{\boldsymbol{\sigma}}_{\boldsymbol{\epsilon}} : \Delta\boldsymbol{\epsilon} + \boldsymbol{T}^{\boldsymbol{\sigma}}_{\varphi^{nl}} \ \Delta\varphi^{nl} \tag{39}$$

where $\boldsymbol{T}^{\boldsymbol{\sigma}}_{\varphi^{nl}}$ denotes the nonlocal tangent modulus. The computation of the tangent stiffness tensor, $\mathbb{T}^{\boldsymbol{\sigma}}_{\boldsymbol{\epsilon}}$, is described in Appendix 1. In the nonlocal formulation, equation (14), the increment of $\gamma^{nl}(\varphi - \varphi^{nl})$ is expressed as follows:

$$\Delta\left[\gamma^{nl}(\varphi - \varphi^{nl})\right] = \boldsymbol{T}^{h}_{\boldsymbol{\epsilon}} : \Delta\boldsymbol{\epsilon} + T^{h}_{\varphi^{nl}} \ \Delta\varphi^{nl} \tag{40}$$

where $\boldsymbol{T}^{h}_{\boldsymbol{\epsilon}}$, and $\boldsymbol{T}^{\boldsymbol{h}}_{\boldsymbol{\varphi^{nl}}}$ denote the nonlocal tangent operators. Technically speaking, HETVAL subroutine, among all nonlocal tangent operators indicated in equations (39) and (40), solely demands for $T^{h}_{\varphi^{nl}}$ which is assigned as the rate of $\gamma^{nl}(\varphi - \varphi^{nl})$ with respect to the nonlocal variable, which is simply derived as:

$$T^{h}_{\varphi^{nl}} = -\gamma^{nl} \tag{41}$$

The return mapping algorithm including viscoelastic correction-prediction and its interactions with the solver and HETVAL is summarized as a flowchart depicted in Figure 1.

Numerical examples and discussions

In this section, the model is examined through finite element computations using a unilaterally notched rectangular plate and an asymmetrically double notched structure, whose dimensions are depicted in Figure 2. In both examples, the material properties are given according to the polyamide 66, which has been earlier calibrated as a local VEVPD model (see Table 3).

As already indicated, in order to perform a nonlocal analysis in a ductile damage model, the nonlocal variable may be derived from the damage variable, D, or from the hardening state variable, r. In this section, first, the model based on the nonlocal damage variable, D^{nl}, is used to investigate the unilaterally notched plate under monotonic strain controlled tensile loading, then its efficiency in controlling the damage localization is discussed. As a second step, the model derived from the nonlocal hardening state variable, r^{nl}, is applied on the structure considering the same loading conditions, and the results are compared with the latter case (related to D^{nl}). Moreover, the influences of the nonlocal parameters, ξ^{nl} and γ^{nl}, on the damage localization are explored through a parametric study. As another numerical example, the asymmetrically double notched structure is used so as to examine the efficiency of the nonlocal model in a more complex geometry case.

The nonlocal framework can be switched to the local model simply by setting the nonlocal parameters ξ^{nl} and γ^{nl} to zero, which enables comparing the responses with those using the nonlocal model. Technically speaking, in highly nonlinear systems, the finite element solver often requires

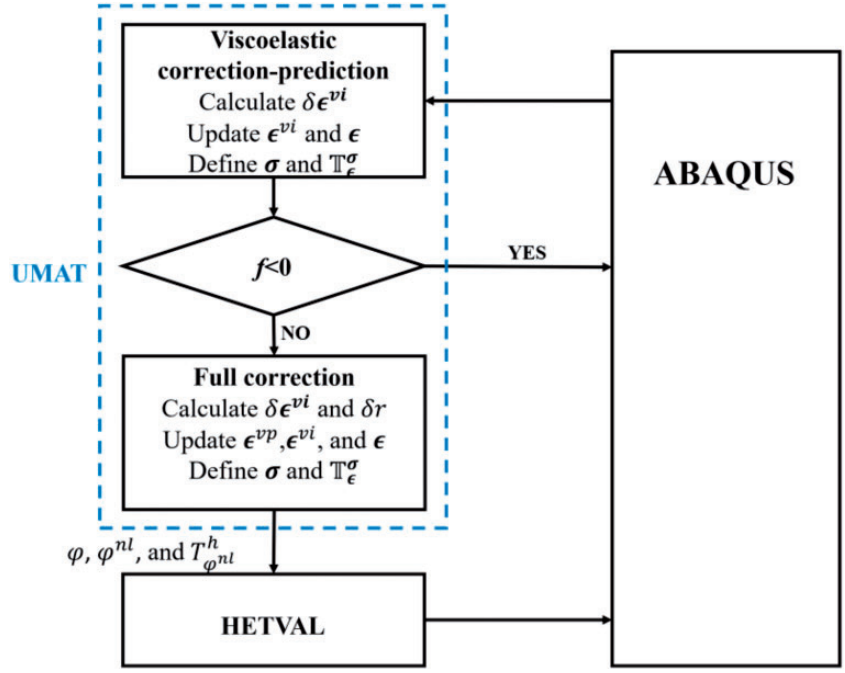

Figure 1. Flowchart of return mapping implementation on UMAT and its interaction with the FE solver and HETVAL subroutine.

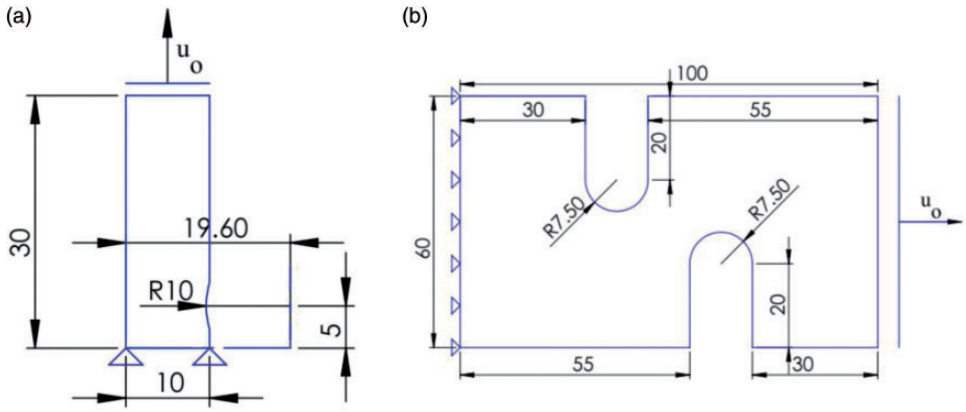

Figure 2. Dimensions of the numerical examples and the given boundary conditions: (a) unilaterally notched plate and (b) asymmetrically double notched plate.

Table 3. Material properties and model parameters for PA66 in 50 percent Relative Humidity (RH) and room temperature (Benaarbia et al., 2019).

Mechanical features	Parameter	Value
Elastic properties:		
Young's modulus	E^e	2731 (MPa)
Poisson ratio	ν	0.3 (–)
Viscoelasticity:		
1st branch:	E^{v1}	9751.44 (MPa)
	τ^{v1}	0.36 (s)
2nd branch:	E^{v2}	19125.64 (MPa)
	τ^{v2}	6.72 (s)
3th branch:	E^{v3}	30855.24 (MPa)
	τ^{v3}	6.38 (s)
4th branch:	E^{v4}	6771.25 (MPa)
	τ^{v4}	128.49 (s)
Viscoplasticity coupled with damage:		
Elastic limit:	R_0	4.76 (MPa)
Hardening model:	H_m	1302.71 (MPa)
	H_p	0.8 (–)
Viscoplastic model	R_{vp}	45.86 (MPa.s$^{P_{vp}}$)
	P_{vp}	0.07 (–)
Damage	S_D	20.03 (MPa)
	β_D	−0.86 (–)

decreasing the time increments to achieve convergent solutions in the "unstable deformation zones". However, in some cases, as in the present study, instabilities in the form of material softening cause sudden changes in the stiffness tensor in the global equilibrium equation of the computational model. In such cases, the time steps become too small and the analysis never ends or converges. To address this issue, a viscous term is added to the global equilibrium that damps sudden changes in the stiffness tensor, as an artificial inertia. In this respect, the "automatic stabilization" in the

finite element solver provides a viscous term with respect to displacement in the global equilibrium equation, which is employed in the present work.

Unilaterally notched plate

In this part, the damage analysis is initially performed using the 4 nodes plane strain fully coupled temperature displacement element type (CPE4T in Abaqus package) in different mesh sizes (300, 602, and 1200 elements). A reference point is set on the plate whose displacement is tied with the upper side allowing to plot the force vs. displacement responses. This aims at extracting more precise information regarding the hardening and softening mechanisms as well as the model behavior beyond the material instability limits.

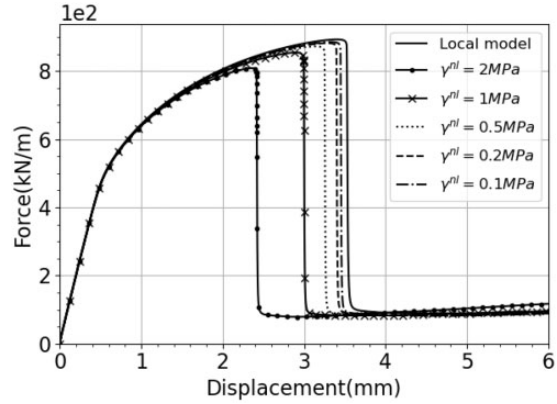

Figure 3. Force displacement curves for the unilaterally notched plate and comparison between local and nonlocal damage models responses for different values of γ^{nl} when $\xi^{nl} = 2\,\text{kN}$ under uniaxial monotonic tensile loading with the displacement rate $\dot{u}_0 = 3\,\text{mms}^{-1}$; the nonlocal model is based on D^{nl}.

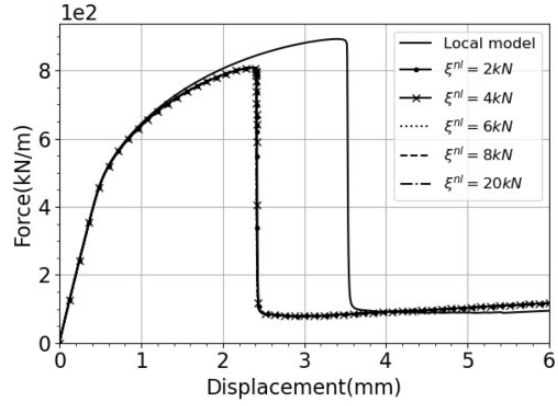

Figure 4. Force displacement curves for the unilaterally notched plate and comparison between local and nonlocal damage models responses for different values of ξ^{nl} when $\gamma^{nl} = 2\,\text{MPa}$ under uniaxial monotonic tensile loading with the displacement rate $\dot{u}_0 = 3\,\text{mms}^{-1}$; the nonlocal model is based on D^{nl}.

In terms of boundary conditions, the plate is subjected to a monotonic displacement-controlled tensile load with a rate of $\dot{u}_0 = 3\,\mathrm{mm\,s^{-1}}$ from one side, and the displacement components are set to zero at the other side (see Figure 2). As already indicated, firstly, the nonlocal analysis is performed based on D^{nl} and is compared with the local model results. The responses are extracted as the force displacement curves in Figure 3 for the local and nonlocal models with different values of γ^{nl} when the structure is meshed by 1200 elements. As previously mentioned, γ^{nl} controls the interaction between D and D^{nl} via the nonlocal associated damage variable Y^{nl} (see Table 2). As observed,

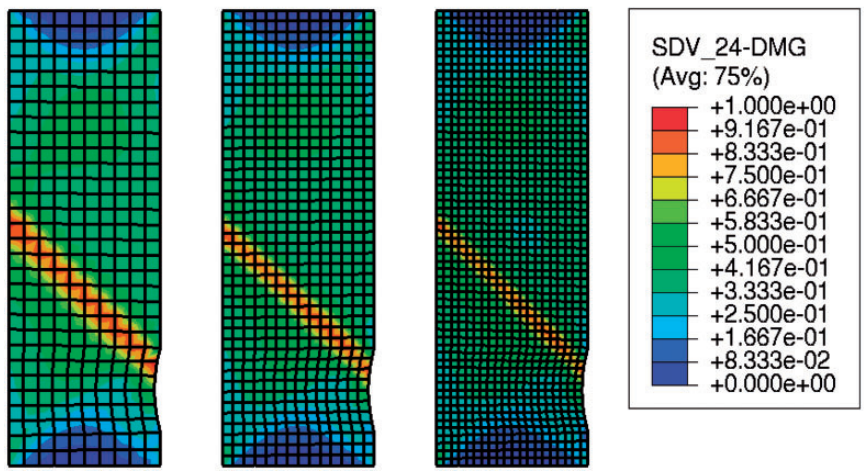

Figure 5. Damage distribution of the unilaterally notched plate using the nonlocal damage model ($\xi^{nl} = 2\,\mathrm{kN}$, $\gamma^{nl} = 2\,\mathrm{MPa}$) under uniaxial monotonic tensile loading with the displacement rate $\dot{u}_0 = 3\,\mathrm{mm\,s^{-1}}$ (three mesh refinements, $N_E = \{300,602,1200\}$); the nonlocal model is based on D^{nl}.

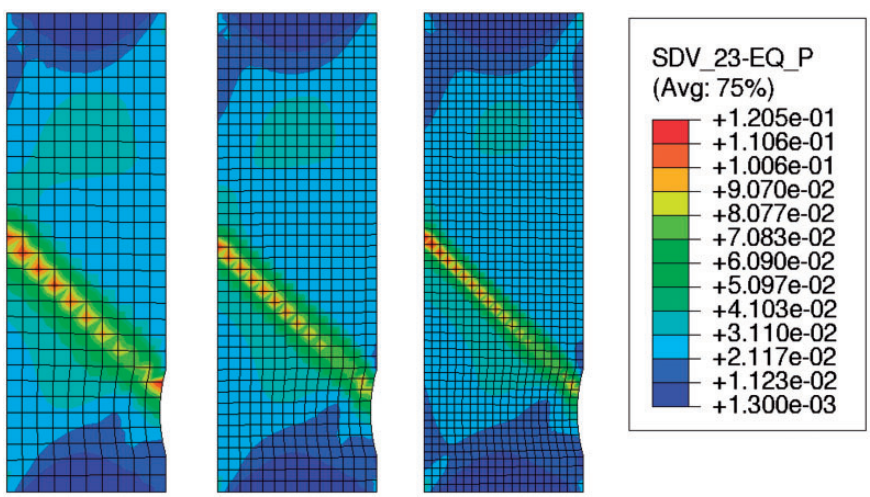

Figure 6. Distribution of the hardening state variable, r, in the unilaterally notched plate using the nonlocal model ($\xi^{nl} = 2\ kN$, $\gamma^{nl} = 2\ MPa$) under uniaxial monotonic tensile loading with the displacement rate $\dot{u}_0 = 3\ mms^{-1}$ (three mesh refinements, N_E={300,602,1200}); the nonlocal model is based on D^{nl}.

introducing nonlocal parameters in this case leads to faster failures compared to the local model. In other words, as the level of interaction with the nonlocal variable increases, the model becomes more unstable and fails earlier.

From the same analysis, force displacement curves are plotted for several levels of ξ^{nl} at a constant value of γ^{nl} in Figure 4. As seen, variation of ξ^{nl} almost has no influence on the material responses because γ^{nl} is not sufficiently large to make a strong interaction between D and D^{nl}, and on the other hand, for the reasons mentioned above, introducing the nonlocal parameters makes the model more unstable than the local framework, and higher values of γ^{nl} are not feasible.

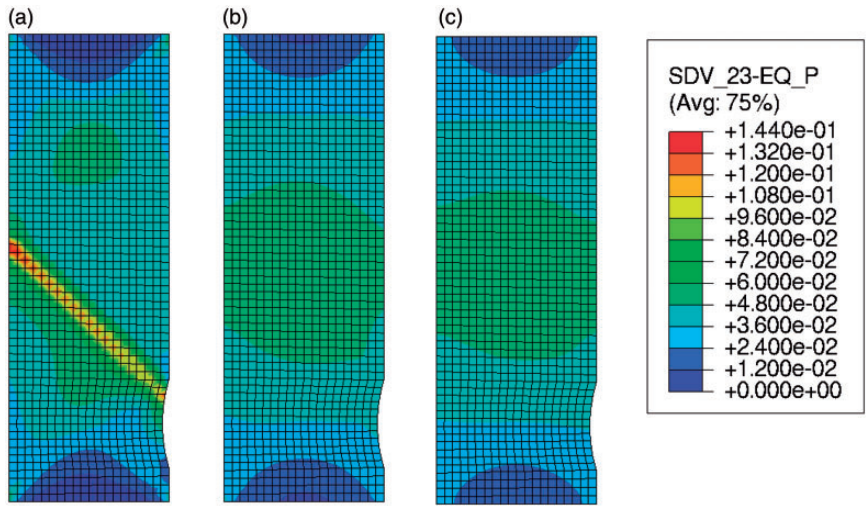

Figure 7. Local and nonlocal variables 2 D maps under monotonic tensile loading: (a) hardening state variable distribution using the local model, (b) hardening state variable distribution using the nonlocal model when $\gamma^{nl} = 5$ GPa and $\xi^{nl} = 6$ kN, and (c) nonlocal variable using the nonlocal model when $\gamma^{nl} = 5\ GPa$ and $\xi^{nl} = 6$ kN; the nonlocal model is based on r^{nl}.

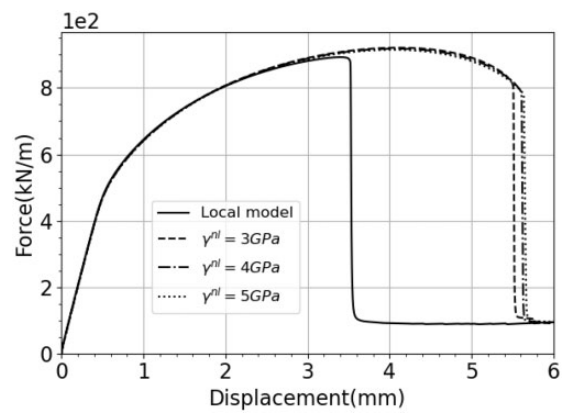

Figure 8. Force displacement curves for the unilaterally notched plate and comparison between local and nonlocal models responses for different values of γ^{nl} when $N_E = 1200$, $\xi^{nl} = 6\ kN$, and $\dot{u}_0 = 3\ mms^{-1}$; the nonlocal model is based on r^{nl}.

Figure 5 provides the damage distribution resulted from the nonlocal damage model in three given mesh sizes, in which the damage, as expected, is localized into the crack zone restricted to a single row of elements as the smallest possible area. Since the damage is coupled with plasticity, and the damage rate is directly related to the hardening state variable rate $\dot{r}$ based on the given evolution laws, the damage localization may stem from the localization of r. Concerning this, the distribution of r, for the nonlocal damage model ($\xi^{nl} = 2\,\text{kN}$, $\gamma^{nl} = 2\,\text{MPa}$), is extracted and depicted as Figure 6. As shown, the hardening state variable is localized into the crack and exhibits mesh sensitivity by refining the mesh, which consequently leads to damage localization. Regarding this, it can be

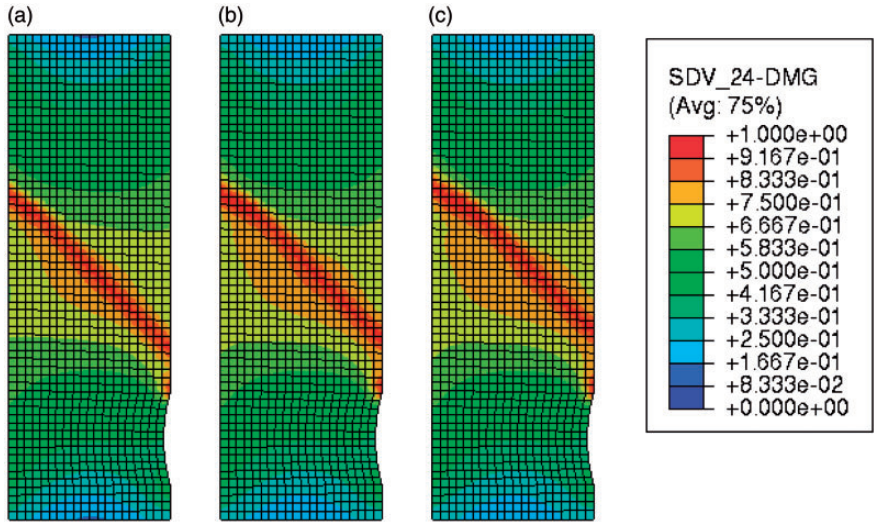

Figure 9. Damage distribution in the unilaterally notched plate under tensile loading ($\dot{u}_0 = 3\ mms^{-1}$) with 1200 elements using: (a) nonlocal model when $\xi^{nl} = 6\ kN$ and $\gamma^{nl} = 3\ GPa$, (b) nonlocal model when $\xi^{nl} = 6\ kN$ and $\gamma^{nl} = 4\ GPa$, and (c) nonlocal model when $\xi^{nl} = 6\ kN$ and $\gamma^{nl} = 5\ GPa$; the nonlocal model is based on r^{nl}.

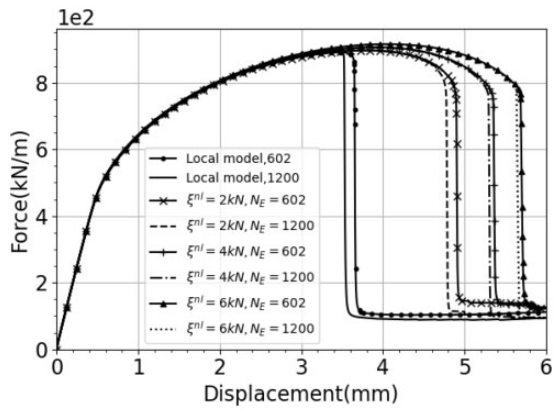

Figure 10. Force displacement curves for unilaterally notched plate and comparison between local and nonlocal models responses for different values of ξ^{nl} when $N_E = \{602, 1200\}$, $\gamma^{nl} = 5\,\text{GPa}$, and $\dot{u}_0 = 3\ mms^{-1}$. By increasing the value of ξ^{nl}, the analysis converges better for different mesh sizes; the nonlocal model is based on r^{nl}.

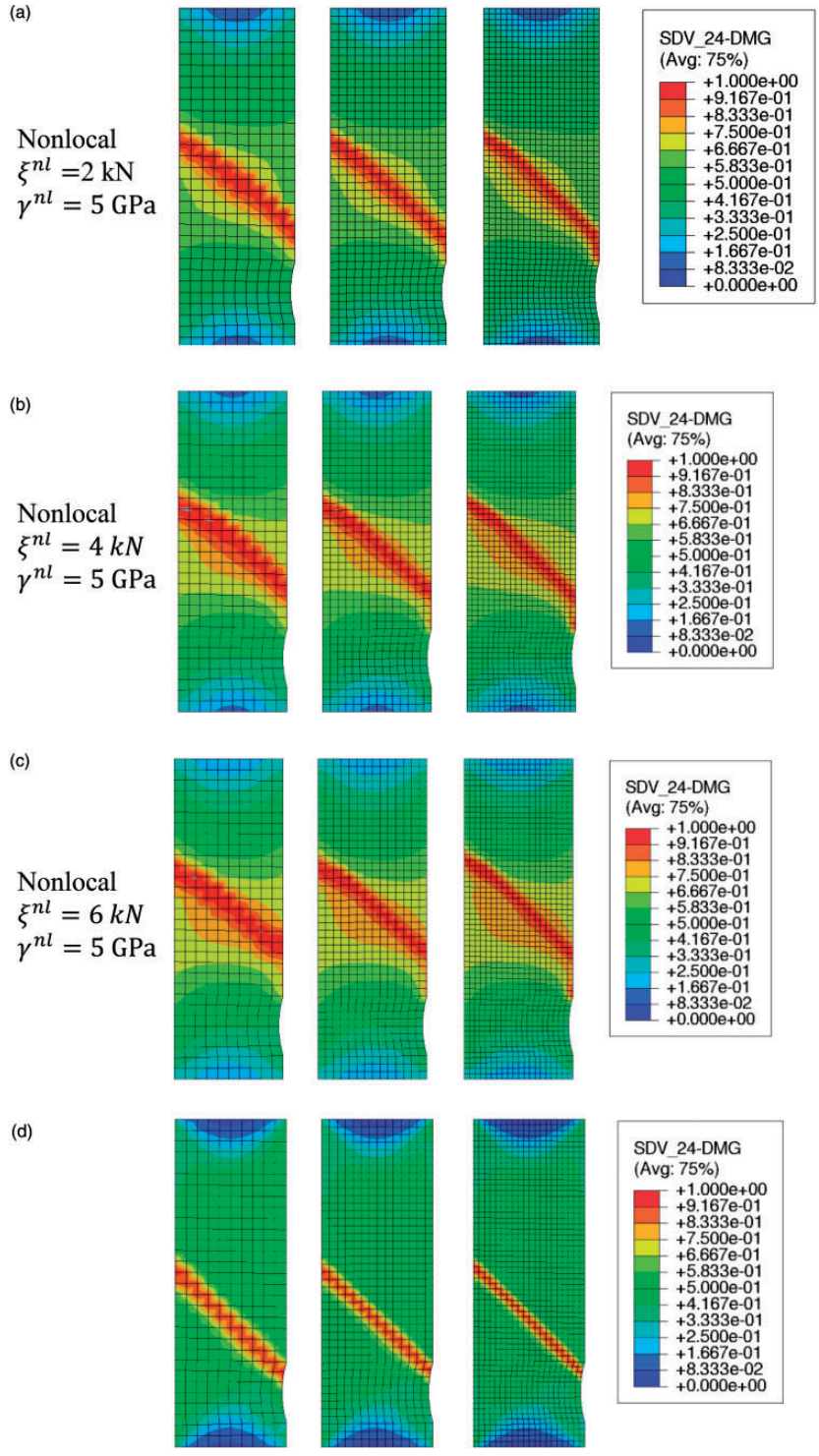

Figure 11. Damage distribution in the unilaterally notched plate meshed by 300, 602, and 1200 elements using nonlocal model with $\gamma^{nl} = 5$ GPa and (a) $\xi^{nl} = 2$ kN, (b) $\xi^{nl} = 4$ kN, (c) $\xi^{nl} = 6$ kN, and comparison with (d) local model; the nonlocal model is based on r^{nl}.

concluded that the nonlocal variable deriving from r may address the damage mesh sensitivity in the FE computations, which is discussed as follows.

As the second option, the nonlocal variable is derived from r, and the nonlocal free energy dictates the nonlocal term R^{nl} into the hardening function R, as indicated in equations (29) and (30). The model is implemented on the considered geometry under same loading and boundary conditions, with the first option. To observe the interaction between local and nonlocal variables (r and r^{nl}), the unilaterally notched structure under tensile load with $\dot{\boldsymbol{u}} = 3\,\mathrm{mm\,s^{-1}}$ is analyzed, then considering the localization time in the local model, the 2D maps of the hardening state variable using the local and nonlocal models (based on r^{nl}) are compared with the distribution of the nonlocal variable in the same time increment (see Figure 7). As seen, r is localized in the local model (Figure 7(a)) while r and r^{nl} on the nonlocal model show no localization or shear band at this stage (Figure 7(b) and (c)). The responses are also exported with respect to γ^{nl} as force displacement curves in Figure 8. As observed, the softening zone in the nonlocal responses are more extended compared to those predicted by the local model and subsequently they drop more smoothly. However, after a certain level of the γ^{nl}, its increase does not yield a significant variation in responses nor in the failure points.

The damage distribution contours visualize a clearer view of the Influence of γ^{nl} on the damage profile (Figure 9). As shown, the bigger the value of γ^{nl} is, the wider damaged area evolves surrounding the crack zone. The model is also examined for different ξ^{nl} in a constant level of interaction ($\gamma^{nl} = 5\,\mathrm{gPa}$) and is depicted in Figure 10. The mesh sensitivity is decreased by an increase in

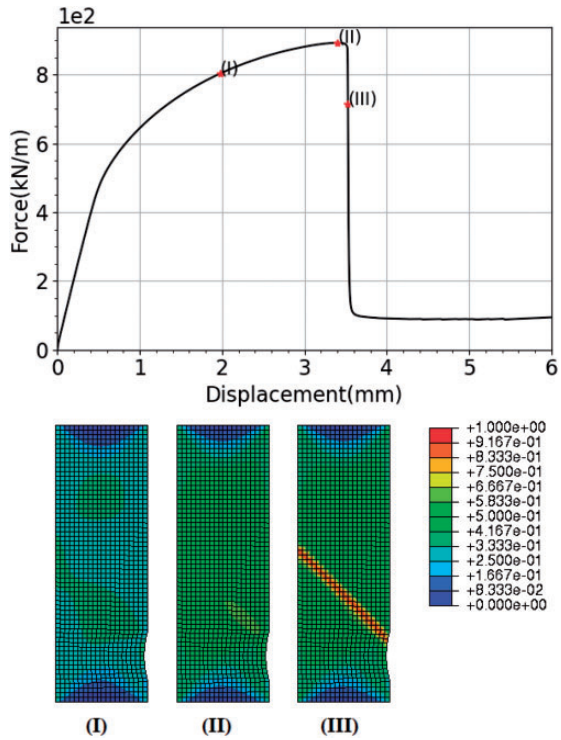

Figure 12. Damage distribution using the local model: (I) before the maximum force and at 90 percent of the peak (II) at the maximum force III) after the maximum force and at 80 percent of the peak.

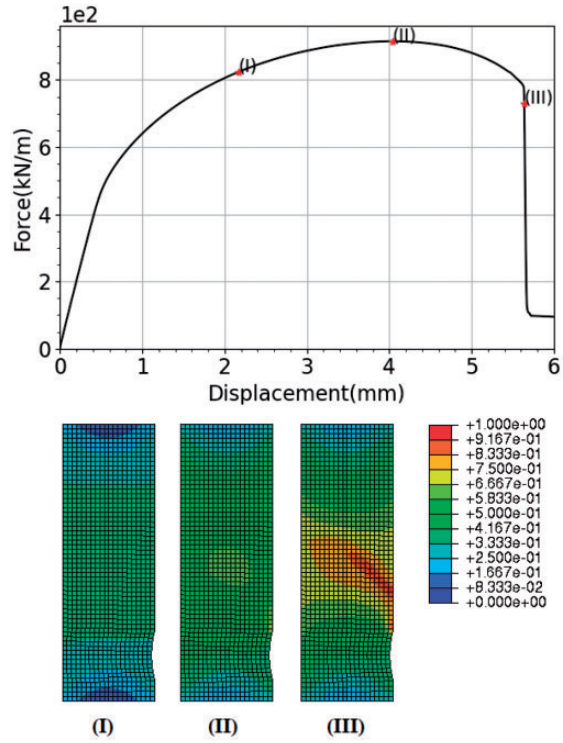

Figure 13. Damage distribution using the nonlocal model with $\xi^{nl} = 6\,\text{kN}$ and $\gamma^{nl} = 5\,\text{GPa}$:I) before the maximum force and at 90 percent of the peak II) at the maximum force III) after the maximum force and at 80 percent of the peak; the nonlocal model is based on r^{nl}.

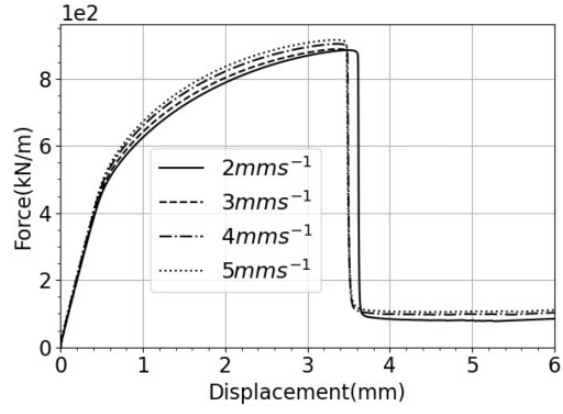

Figure 14. Force displacement curves obtained from the local model for unilaterally notched plate under different loading rates.

ξ^{nl}, and the softening zone becomes smoother, which leads to failure in higher deformation levels. The aforementioned notion is confirmed with the damage distribution contours in three different mesh sizes $N_E = \{300,602,1200\}$ for several values of ξ^{nl} (see Figure 11). In the local model contour, as seen also earlier, the damage is localized into a single row of elements and shows mesh sensitivity by changing the mesh size. This issue is addressed by introducing the nonlocal parameters into the model. The damage in the vicinity of the crack is progressively evolved by an increase in ξ^{nl}, and the damage profile remains identical for different mesh sizes in the higher level of γ^{nl}.

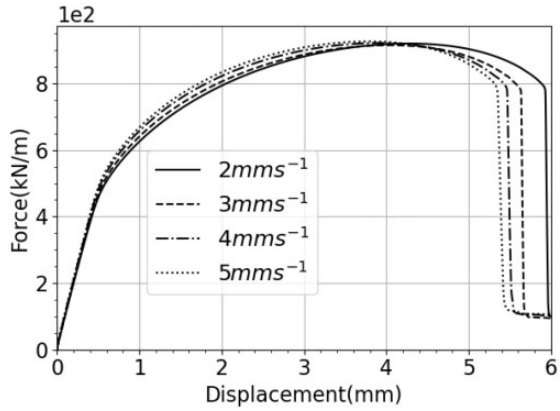

Figure 15. Force displacement curves obtained from the nonlocal model (with $\xi^{nl} = 6$ kN and $\gamma^{nl} = 5$ GPa) for the unilaterally notched plate under different loading rates; the nonlocal model is based on r^{nl}.

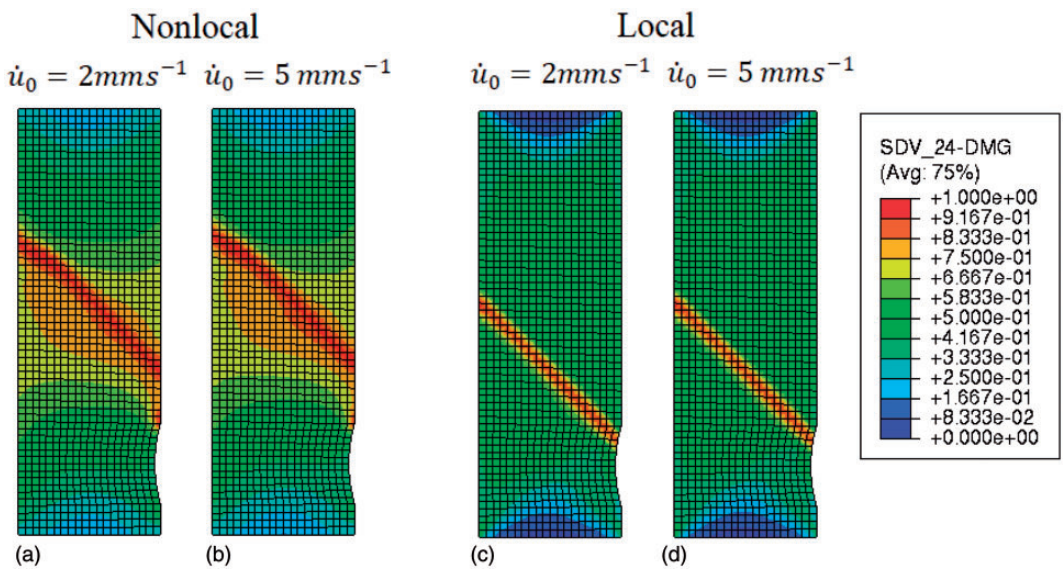

Figure 16. Damage distribution in the unilaterally notched plate with 1200 elements using nonlocal model when $\xi^{nl} = 6$ *kN* and γ^{nl}=5 GPa under displacement rates: (a) $u_0 = 2\,\text{mm}\,\text{s}^{-1}$, (b) $u_0 = 5\ mms^{-1}$ and using the local model under displacement rates: (c) $\dot{u}_0 = 2mms^{-1}$, (d) $\dot{u}_0 = 5\ mms^{-1}$; the nonlocal model is based on r^{nl}.

In order to investigate how the nonlocal model affects and governs the damage development within the structure prior and after the reaction force peak, three spots are taken into consideration: I) the first spot at 90% of the peak prior to it, II) the second spot at the peak, and III) the third one at its 80% after the peak, at which the damage distributions are compared for the local and nonlocal models and illustrated in the Figures 12 and 13. As observed, as the material approaches the instability region, the discrepancies in damage distributions between the local and nonlocal models become more pronounced, particularly after the reaction force peak.

As the material is defined through the VEVPD rheological model, the change in the loading rate necessarily affects the material behavior and the related damage distribution. Following this, the structure is subjected to different loading rates and the force displacement curves are explored for local and nonlocal models in the Figures 14 and 15. As observed, the curves obtained from the local case are mostly affected by the loading rate in the hardening zone, and their failure point is slightly shifted forward by an increase in the rate (see Figure 14). However, the rate effect is more significant in the nonlocal model, particularly at the failure points, where the higher rate yields sharper softening regions and subsequent earlier failures (see Figure 15). The damage distribution is extracted for $\dot{u}_0 = \{2,5\} mm\ s^{-1}$ and presented in the Figure 16. As seen, for the local model, no difference is

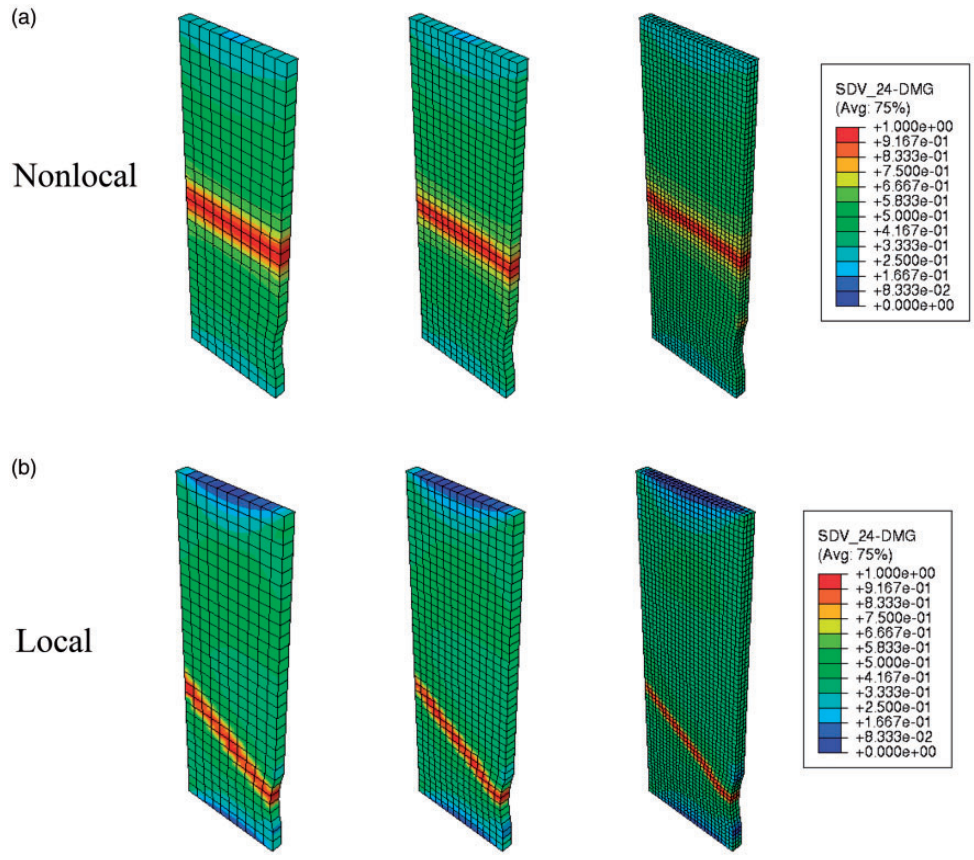

Figure 17. Damage distribution in the unilaterally notched plate with 300, 602, and 5625 elements using: (a) nonlocal model when $\xi^{nl} = 6\ kN$ and $\gamma^{nl} = 5GPa$, (b) local model; the nonlocal model is based on r^{nl}.

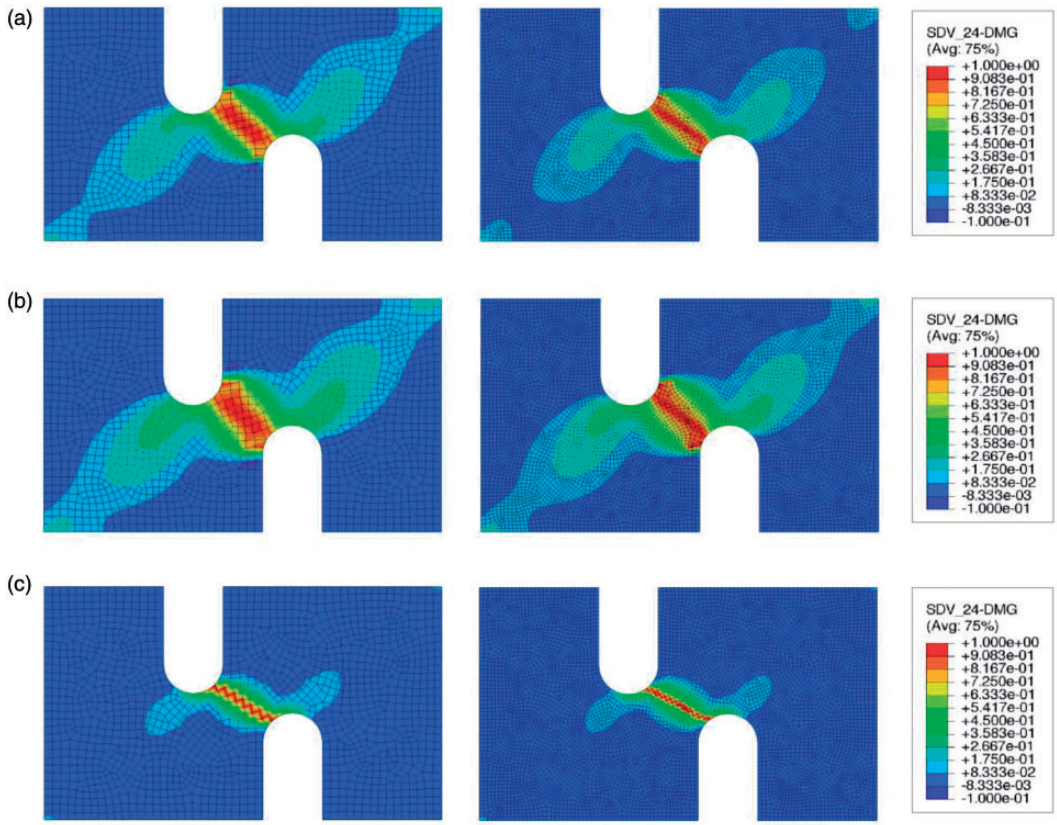

Figure 18. Damage distribution in the asymmetrically double notched plate under uniaxial tensile load with the displacement rate $\dot{u}_0 = 10\ mms^{-1}$ meshed by 1555 and 6346 elements using the nonlocal model with $\gamma^{nl} = 3\ GPa$ and (a) $\xi^{nl} = 4\ kN$, (b) $\xi^{nl} = 6\ kN$ and comparison with (c) local model; the nonlocal model is based on r^{nl}.

observable under given loading rates. However, in the nonlocal model, the damaged region surrounding the crack is slightly reduced and localized toward the crack by an increase in the displacement rate.

In order to capture the effects of transverse deformation in the thickness direction, the unilaterally notched structure is studied in a 3D setup considering a thickness of $1\ mm$. The structure is meshed using the 8 nodes thermally coupled brick element type (C3D8T). In terms of the boundary conditions, all displacement components are bounded at the bottom, and a monotonic tensile load ($\dot{u}_0 = 3\ mm\ s^{-1}$) is set to the top. The damage analysis results are extracted as contours and depicted in Figure 17. As observed, the crack inclination is decreased compared to the plane strain case, which it is reduced more drastically for the nonlocal model (see Figure 17(a)).

Asymmetrically double notched rectangular plate

Based on the results and discussions in the previous section, the nonlocal model employing r^{nl} works more efficiently than the first option using D^{nl} and is thereby preferred to implement as the nonlocal model on the asymmetrically double notched structure (see Figure 2). For the 2D case, the structure is meshed via 3 and 4 nodes plane strain temperature-displacement elements (CPE3T, CPE4T) in

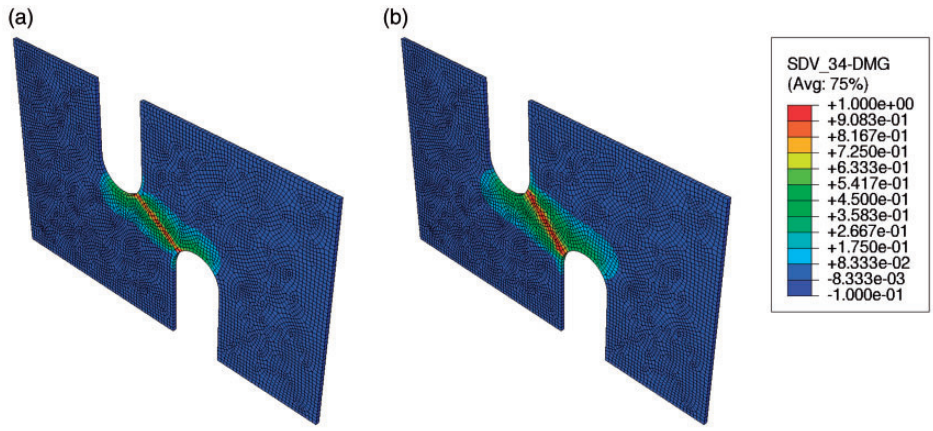

Figure 19. Damage distribution in the asymmetrically double notched plate under uniaxial tensile load with the displacement rate $\dot{u}_0 = 10\ mms^{-1}$ meshed by 6444 elements using (a) local model, and (b) nonlocal model with $\gamma^{nl} = 3\ GPa$ and $\xi^{nl} = 6\ kN$; the nonlocal model is based on r^{nl}.

two mesh sizes (N_E={1555,6346}). The plate is subjected to the monotonic uniaxial tensile load with $\dot{u}_0 = 10\ mm\ s^{-1}$ from the right side, and the displacement at the left side is bounded to zero. The damage contours are extracted for the local and nonlocal models with $\xi^{nl} = \{4\ kN, 6\ kN\}$ and displayed in Figure 18. As seen, an increase in ξ^{nl} leads to change in the damage profile and thicken the shear band (Figure 18(a) and (b)). While, for the local case (Figure 18(c)), the damage is mostly localized into the crack zone and shows the tendency to occupy the minimum possible area. The aforementioned structure with a thickness of $1\,mm$, under the same loading and boundary conditions, is examined through the 3D element, C3D8T. The damage distribution is provided for the local and nonlocal model ($\xi^{nl} = 6\ kN,\ \gamma^{nl} = 3\ GPa$) and shown in the Figure 19. In the 3D case, the damage localization is well addressed. In comparison with the 2D case, the damage profile is affected by the Poisson's effect, which leads to a less defused damage profile with a narrower crack zone.

Conclusions and perspectives

A gradient enhanced thermodynamically based framework was proposed towards investigating the polyamide 66 (PA66) mechanical behavior in the highly damaged levels and address the spurious damage localization leading to the macroscopic failure as well as the consequent mesh sensitivity in the FE computations. To this end, the thermodynamics of irreversible processes and the Generalized Standard Materials formalism were employed to derive the constitutive equations. A specific nonlocal formulation for the thermodynamic potential was considered and then enhanced based on two cases regarding the nonlocal state variable: nonlocal damage, and nonlocal hardening state variable. The constitutive laws were integrated through the convex cutting plane as a return mapping algorithm and implemented within the finite element framework through a user defined material subroutine. The analogy between the steady state heat equation and the nonlocal formulation allowed to introduce the implicit nonlocal equation into the FE solver. Considering two nonlocal variable cases, numerical examples were presented to perform a parametric study and examine the nonlocal model efficiency in controlling the damage localization.

Investigation of the numerical examples revealed that r^{nl} is a proper nonlocal variable to control the damage localization and to improve the mesh sensitivity compared to D^{nl} in FE computations. In other words, employing D^{nl} as the nonlocal variable does not enable the model to control the damage localization while a spurious plasticity localization appears during the material softening. The nonlocal model based on r^{nl} yielded mesh objective responses and exhibited the capability of investigating the material behavior in higher levels of damage during material softening stages. The mesh objectivity of the results has been improved for the higher values of the nonlocal parameters γ^{nl} and ξ^{nl}. However, beyond a certain level of nonlocal parameters, no significant effect on the solutions is observed.

Up to now, this research has proposed a nonlocal framework for isotropic semicrystalline polymers which paves the path for micromechanical modelling and investigating the damage behaviors in the fiber reinforced polymers (Chatzigeorgiou et al., 2015, 2016), in which the nonlocal phenomena occur under small strains. In addition, the present model needs to account for the temperature effects to enhance its capability for capturing the physical behavior of polymers under harsh environments. To this end, a thermomechanical nonlocal damage model for polymeric based composites must be developed via considering the self-dissipation and associated thermomechanical coupling sources which have an undeniable influence on the material deformation mechanisms and the damage growth (Benaarbia et al., 2015; Chatzigeorgiou et al., 2016). Moreover, the present model can be more comprehensive by incorporating the hydrostatic pressure effect and the ratio of compressive to tensile elastic limits into the yield function. In this regard, the given von Mises criterion based on the second invariant of the deviatoric stress, J_2, can be extended to a I_1–J_2 function which also considers the difference between the compressive and tensile elastic limits (Ghorbel, 2008; Raghava et al., 1973). As another perspective, the effect of relative humidity on the semicrystalline polymers deformation and nonlinear mechanisms can be investigated within the nonlocal model. As the mater of fact, relative humidity affects the glass transition temperature in polymers which causes exhibiting rubbery behavior in the nominal working temperatures (Benaarbia et al., 2016). In terms of the experimental development, the present model will be first calibrated experimentally and then validated through mechanical tests (Marguères and Meraghni, 2013). In addition, the nonlocal parameter in function of the length scale according to the dominant damage mechanisms requires to be identified via an inverse mixed numerical-experimental optimization approach, which accounts for the microstructural characteristics at the macro scale (Geers et al., 1999, 1999).

Highlights

- Formulation of a nonlocal gradient enhanced constitutive model for numerically capturing the ductile damage localization in semicrystalline polymers coupling viscoelasticity and viscoplasticity.
- Efficiency evaluation of the gradient enhanced model in predicting the damage localization when using the nonlocal damage or the nonlocal hardening state variable.
- The use of the nonlocal hardening state variable to explore the semicrystalline polymers mechanical behaviors within the highly damaged regions under strain softening.

Declaration of conflicting interests

The author(s) declared no potential conflicts of interest with respect to the research, authorship, and/or publication of this article.

Funding

The author(s) received no financial support for the research, authorship, and/or publication of this article.

ORCID iD

Fodil Meraghni https://orcid.org/0000-0002-5043-8700

References

Al-Rub RKA and Voyiadjis GZ (2004) Analytical and experimental determination of the material intrinsic length scale of strain gradient plasticity theory from micro- and nano-indentation experiments. *International Journal of Plasticity* 20(6): 1139–1182.

Arif MF, Saintier N, Meraghni F, et al. (2014) Multiscale fatigue damage characterization in short glass fiber reinforced polyamide-66. *Composites Part B: Engineering* 61: 55–65.

Arruda EM and Boyce MC (1993) A three-dimensional constitutive model for the large stretch behavior of rubber elastic materials. *Journal of the Mechanics and Physics of Solids* 41(2): 389–412.

Bažant ZP (1976) Instability, ductility, and size effect in Strain-Softening concrete. *Journal of the Engineering Mechanics Division* 102(2): 331–344.

Bažant ZP, Belytschko TB and Chang TP (1984) Continuum theory for strain-softening. *Journal of Engineering Mechanics* 110(12): 1666–1692.

Bazant ZP and Lin FB (1988) Nonlocal smeared cracking model for concrete fracture. *Journal of Structural Engineering* 114(11): 2493–2510.

Benaarbia A, Chatzigeorgiou G, Kiefer B, et al. (2019) A fully coupled thermo-viscoelastic-viscoplastic-damage framework to study the cyclic variability of the Taylor-Quinney coefficient for semi-crystalline polymers. *International Journal of Mechanical Sciences* 163: 105128.

Benaarbia A, Chrysochoos A and Robert G (2014) Influence of relative humidity and loading frequency on the PA6.6 cyclic thermomechanical behavior: Part I. Mechanical and thermal aspects. *Polymer Testing* 40: 290–298.

Benaarbia A, Chrysochoos A and Robert G (2014) Kinetics of stored and dissipated energies associated with cyclic loadings of dry polyamide 6.6 specimens. *Polymer Testing* 34: 155–167.

Benaarbia A, Chrysochoos A and Robert G (2015) Thermomechanical behavior of PA6.6 composites subjected to low cycle fatigue. *Composites Part B: Engineering* 76: 52–64.

Benaarbia A, Chrysochoos A and Robert G (2016) Thermomechanical analysis of the onset of strain concentration zones in wet polyamide 6.6 subjected to cyclic loading. *Mechanics of Materials* 99: 9–25.

Benaarbia A, Rae Y and Sun W (2018) Unified viscoplasticity modelling and its application to fatigue-creep behaviour of gas turbine rotor. *International Journal of Mechanical Sciences* 136: 36–49.

Billon N (2012) New constitutive modeling for time-dependent mechanical behavior of polymers close to glass transition: Fundamentals and experimental validation. *Journal of Applied Polymer Science* 125(6): 4390–4401.

Borst dRR, Geers MM, Peerlings RR, et al. (1998) Some remarks on gradient and nonlocal damage theories. *Studies in Applied Mechanics* 46: 223–236.

Borst RRD and Verhoosel CC (2016) Gradient damage vs phase-field approaches for fracture: Similarities and differences. *Computer Methods in Applied Mechanics and Engineering* 312: 78–94.

Boyce MC, Parks DM and Argon AS (1988) Large inelastic deformation of glassy polymers. Part I: Rate dependent constitutive model. *Mechanics of Materials* 7(1): 15–33.

Breemen vLL, Klompen EE, Govaert LL, et al. (2011) Extending the EGP constitutive model for polymer glasses to multiple relaxation times. *Journal of the Mechanics and Physics of Solids* 59(10): 2191–2207.

Brepols T, Wulfinghoff S and Reese S (2017) Gradient-extended two-surface damage-plasticity: Micromorphic formulation and numerical aspects. *International Journal of Plasticity* 97: 64–106.

Buckley C and Jones D (1995) Glass-rubber constitutive model for amorphous polymers near the glass transition. *Polymer* 36(17): 3301–3312.

Chaboche J-L (1997) Thermodynamic formulation of constitutive equations and application to the viscoplasticity and viscoelasticity of metals and polymers. *International Journal of Solids and Structures* 34(18): 2239–2254.

Chaboche J (2008) A review of some plasticity and viscoplasticity constitutive theories. *International Journal of Plasticity* 24(10): 1642–1693.

Chatzigeorgiou G, Charalambakis N, Chemisky Y, et al. (2016) Periodic homogenization for fully coupled thermomechanical modeling of dissipative generalized standard materials. *International Journal of Plasticity* 81: 18–39.

Chatzigeorgiou G, Chemisky Y and Meraghni F (2015) Computational micro to macro transitions for shape memory alloy composites using periodic homogenization. *Smart Materials and Structures* 24(3): 035009.

Chen D-L, Yang P-F and Lai Y-S (2012) A review of three-dimensional viscoelastic models with an application to viscoelasticity characterization using nanoindentation. *Microelectronics Reliability* 52(3): 541–558.

Dimitrijevic BJ and Hackl K (2008) A method for gradient enhancement of continuum damage models. *Technische Mechanik – European Journal of Engineering Mechanics* 28(1): 43–52.

Dimitrijevic BJ and Hackl K (2011) A regularization framework for damage–plasticity models via gradient enhancement of the free energy. *International Journal for Numerical Methods in Biomedical Engineering* 27(8): 1199–1210.

Engelen RA, Geers MG and Baaijens FP (2003) Nonlocal implicit gradient-enhanced elasto-plasticity for the modelling of softening behaviour. *International Journal of Plasticity* 19(4): 403–433.

Forest S (2009) Micromorphic approach for gradient elasticity, viscoplasticity, and damage. *Journal of Engineering Mechanics* 135(3): 117–131.

Geers M, Borst RD and Peijs T (1999) Mixed numerical-experimental identification of non-local characteristics of random-fibre-reinforced composites. *Composites Science and Technology* 59(10): 1569–1578.

Geers MM, Borst DRR, Brekelmans WM, et al. (1999) Validation and internal length scale determination for a gradient damage model: application to short glass-fibre-reinforced polypropylene. *International Journal of Solids and Structures* 36(17): 2557–2583.

Geers MM, Peerlings RR, Brekelmans WM, et al. (2000) Phenomenological nonlocal approaches based on implicit gradient-enhanced damage. *Acta Mechanica* 144(1–2): 1–15.

Germain P, Suquet P and Nguyen QS (1983) Continuum thermomechanics. *Journal of Applied Mechanics* 50(4b): 1010–1020.

Ghorbel E (2008) A viscoplastic constitutive model for polymeric materials. *International Journal of Plasticity* 24(11): 2032–2058.

Govaert LL, Timmermans PP and Brekelmans WM (2000) The influence of intrinsic strain softening on strain localization in polycarbonate: Modeling and experimental validation. *Journal of Engineering Materials and Technology* 122(2): 177–185.

Gudimetla MR and Doghri I (2017) A finite strain thermodynamically-based constitutive framework coupling viscoelasticity and viscoplasticity with application to glassy polymers. *International Journal of Plasticity* 98: 197–216.

Halphen B and Nguyen QS (1975) On the generalized standards materials (in French). *Journal de Mécanique* 14: 39–63.

Hortig C (2010) Local and non-local thermomechanical modeling and finite-element simulation of high-speed cutting.

Jirásek M (1998) Nonlocal models for damage and fracture: Comparison of approaches. *International Journal of Solids and Structures* 35(31–32): 4133–4145.

Jirásek M (2002) Objective modeling of strain localization. *Revue Française de Génie Civil* 6(6): 1119–1132.

Jirásek M (2007) Nonlocal damage mechanics. *Revue Européenne de Génie Civil* 11(7-8): 993–1021.

Jirásek M, Rolshoven S and Grassl P (2004) Size effect on fracture energy induced by non-locality. *International Journal for Numerical and Analytical Methods in Geomechanics* 28(78): 653–670.

Juan C Simo TJH (1997) *Computational Inelasticity*. s.l.:Springer.

Kachanov LM (1958) *On the creep fracture time*. s.l.:izv akad. *Nauk USSR Otd. Tech* 8: 26–31. (in Russian).

Kiefer B, Waffenschmidt T, Sprave L, et al. (2018) A gradient-enhanced damage model coupled to plasticity – Multi-surface formulation and algorithmic concepts. *International Journal of Damage Mechanics* 27(2): 253–295.

Klompen EE, Engels TT, Govaert LL, et al. (2005) Modeling of the postyield response of glassy polymers: Influence of thermomechanical history. *Macromolecules* 38(16): 6997–7008.

Krairi A and Doghri I (2014) A thermodynamically-based constitutive model for thermoplastic polymers coupling viscoelasticity, viscoplasticity and ductile damage. *International Journal of Plasticity* 60: 163–181.

Launay A, Maitournam MH, Marco Y, et al. (2011) Cyclic behaviour of short glass fibre reinforced polyamide: Experimental study and constitutive equations. *International Journal of Plasticity* 27(8): 1267–1293.

Lemaitre J and Chaboche J-L (1990) *Mechanics of Solid Materials*. Cambridge: Cambridge University Press.

Marguères P and Meraghni F (2013) Damage induced anisotropy and stiffness reduction evaluation in composite materials using ultrasonic wave transmission. *Composites Part A: Applied Science and Manufacturing* 45: 134–144.

Miehe C, Aldakheel F and Raina A (2016) Phase field modeling of ductile fracture at finite strains: a variational gradient-extended plasticity-damage theory. *International Journal of Plasticity* 84: 1–32.

Miehe C, Hofacker M and Welschinger F (2010) A phase field model for rate-independent crack propagation: Robust algorithmic implementation based on operator splits. *Computer Methods in Applied Mechanics and Engineering* 199(45–48): 2765–2778.

Nouri H, Meraghni F and Lory P (2009) Fatigue damage model for injection-molded short glass fibre reinforced thermoplastics. *International Journal of Fatigue* 31(5): 934–942.

Ortiz M and Simo JC (1986) An analysis of a new class of integration algorithms for elastoplastic constitutive relations. *International Journal for Numerical Methods in Engineering* 23(3): 353–366.

Ostwald R, Kuhl E and Menzel A (2019) On the implementation of finite deformation gradient-enhanced damage models. *Computational Mechanics* 64(3): 847–877.

Pamin J (1994) *Gradient-dependent plasticity in numerical simulation of localization phenomena*. PhD Thesis.

Papanicolaou G and Zaoutsos S (2011) Viscoelastic constitutive modeling of creep and stress relaxation in polymers and polymer matrix composites. In: *Creep and Fatigue in Polymer Matrix Composites (Second Edition)*. Woodhead Publishing, pp. 3–47.

Peerlings RR, Geers MM, Borst dRR, et al. (2001) A critical comparison of nonlocal and gradient-enhanced softening continua. *International Journal of Solids and Structures* 38(44–45): 7723–7746.

Pijaudier-Cabot G and Bažant ZP (1987) Nonlocal damage theory. *Journal of Engineering Mechanics* 113(10): 1512–1533.

Praud F, Chatzigeorgiou G, Bikard J, et al. (2017) Phenomenological multi-mechanisms constitutive modelling for thermoplastic polymers, implicit implementation and experimental validation. *Mechanics of Materials* 114: 9–29.

Praud F, Chatzigeorgiou G and Meraghni F (2021) Fully integrated multi-scale modelling of damage and time-dependency in thermoplastic-based woven composites. *International Journal of Damage Mechanics* 30(2): 163–195.

Qidwai MA and Lagoudas DC (2000) Numerical implementation of a shape memory alloy thermomechanical constitutive model using return mapping algorithms. *International Journal for Numerical Methods in Engineering* 47(6): 1123–1168.

Rabotnov YN (1968) *Creep Rupture*. Stanford: Springer.

Raghava RS, Caddell RM and Yeh GSY (1973) The macroscopic yield behaviour of polymers. *Journal of Materials Science* 8(2): 225–232.

Rodas CO, Zaïri F and Naït-Abdelaziz M (2014) A finite strain thermo-viscoelastic constitutive model to describe the self-heating in elastomeric materials during low-cycle fatigue. *Journal of the Mechanics and Physics of Solids* 64(64): 396–410.

Saanouni K and Hamed M (2013) Micromorphic approach for finite gradient-elastoplasticity fully coupled with ductile damage: Formulation and computational aspects. *International Journal of Solids and Structures* 50(14–15): 2289–2309.

Seupel A, Hütter G and Kuna M (2018) An efficient FE-implementation of implicit gradient-enhanced damage models to simulate ductile failure. *Engineering Fracture Mechanics* 199: 41–60.
Silling S (2000) Reformulation of elasticity theory for discontinuities and Long-Range forces. *Journal of the Mechanics and Physics of Solids* 48(1): 175–209.
Silling S and Lehoucq R (2010) Peridynamic Theory of Solid Mechanics. In: *Advances in Applied Mechanics*. Elsevier, pp. 73–168.
Simo JC and Hughes TJ (2006) *Computational Inelasticity*. New York, NY: Springer Science & Business Media.
Simone A, Askes H and Sluys LJ (2004) Incorrect initiation and propagation of failure in non-local and gradient-enhanced media. *International Journal of Solids and Structures* 41(2): 351–363.
Tervoort TT, Smit RR, Brekelmans WM, et al. (1998) A constitutive equation for the elasto-viscoplastic deformation of glassy polymers. *Mechanics of Time-Dependent Materials* 1(3): 269–291.
Wu L, Noels L, Adam L, et al. (2013) *Non-Local Damage-Enhanced MFH for Multiscale Simulations of Composites*. ■: ■, pp.115–121.

Appendix 1

Backward Euler time discretization

An implicit backward Euler scheme is imposed on the governing equations, particularly on the nullity conditions ϕ^{vp} and $\boldsymbol{\phi}^{vi}$, so as to discretize them into n time steps, Δt:

$$\boldsymbol{\phi}^{vi}_{n+1} = \frac{1}{1-D_{n+1}}\left(\mathbb{V}^{vi}\right)^{-1} : \boldsymbol{\sigma}^{vi}_{(n+1)} - \frac{\Delta\boldsymbol{\epsilon}^{vi}}{\Delta t}, \text{ with } \Delta\boldsymbol{\epsilon}^{vi} = \boldsymbol{\epsilon}^{vi}_{n+1} - \boldsymbol{\epsilon}^{vi}_{n} \tag{42}$$

$$\phi^{vp}_{n+1} = \left\langle \frac{f_{n+1}}{R_{vp}} \right\rangle_{+}^{P_{vp}^{-1}} - \frac{\Delta r}{\Delta t}, \text{ with } \Delta r = r_{n+1} - r_n \tag{43}$$

$$f_{n+1} = \frac{\sigma^{eq}_{n+1}}{(1-D_{n+1})} - R_{n+1} - R_0 \tag{44}$$

$$\boldsymbol{\sigma}_{n+1} = (1-D_{n+1})\mathbb{C}^{e} : \left(\boldsymbol{\epsilon}_{n+1} - \boldsymbol{\epsilon}^{vp}_{n+1} - \sum_{j=1}^{N_v} \boldsymbol{\epsilon}^{vj}_{n+1}\right) \tag{45}$$

$$\boldsymbol{\sigma}^{vi}_{n+1} = \boldsymbol{\sigma}_{n+1} - (1-D_{n+1})\mathbb{C}^{vi} : \boldsymbol{\epsilon}^{vi}_{n+1}. \tag{46}$$

Linearization according to the convex cutting plane approach

In this section, in order to solve the time discretized relations, the return mapping algorithm is implemented on the constitutive equations, in which the gradients of the flow are ignored for more simplicity (Ortiz and Simo, 1986). The flow equations can be linearized based on the given evolution laws (see Table 1):

$$\delta\boldsymbol{\epsilon}^{vp} = \boldsymbol{\Lambda}_{vp}\delta r, \ \ \delta D = \Lambda_D \delta r \tag{47}$$

where, from now on, the indices n and k are ignored. Based on equation (47), the linearization of the stress, the viscoelastic conjugate state variable, the yield function, and the viscoelastic and viscoplastic criteria (see Table 1) are derived as:

- stress tensor linearization:

$$\begin{aligned}\delta\boldsymbol{\sigma} &= \frac{\partial\boldsymbol{\sigma}}{\partial D}\delta D + \frac{\partial\boldsymbol{\sigma}}{\partial\boldsymbol{\epsilon}} : \delta\boldsymbol{\epsilon} + \frac{\partial\boldsymbol{\sigma}}{\partial\boldsymbol{\epsilon}^{vp}} : \delta\boldsymbol{\epsilon}^{vp} + \frac{\partial\boldsymbol{\sigma}}{\partial\boldsymbol{\epsilon}^{vi}} : \delta\boldsymbol{\epsilon}^{vi} \\ &= \boldsymbol{B}^e\delta D + \mathbb{B}^d : \delta\boldsymbol{\epsilon} - \mathbb{B}^d : \delta\boldsymbol{\epsilon}^{vp} - \mathbb{B}^d : \sum_{j=1}^{N_v}\delta\boldsymbol{\epsilon}^{vj} \\ &= \boldsymbol{B}^e\Lambda_D\delta r + \mathbb{B}^d : \delta\boldsymbol{\epsilon} - \mathbb{B}^d : \boldsymbol{\Lambda}_{vp}\delta r - \mathbb{B}^d : \sum_{j=1}^{N_v}\delta\boldsymbol{\epsilon}^{vj} \\ &= \boldsymbol{B}^p\delta r + \mathbb{B}^d : \delta\boldsymbol{\epsilon} - \mathbb{B}^d : \sum_{j=1}^{N_v}\delta\boldsymbol{\epsilon}^{vj} \end{aligned} \tag{48}$$

  with

$$\boldsymbol{B}^e = -\mathbb{C}^e : \left(\boldsymbol{\epsilon} - \boldsymbol{\epsilon}^{vp} - \sum_{j=1}^{N_v}\boldsymbol{\epsilon}^{vj}\right) \tag{49}$$

$$\mathbb{B}^d = (1-D)\mathbb{C}^e \tag{50}$$

$$\boldsymbol{B}^p = \boldsymbol{B}^e\Lambda_D - \mathbb{B}^d : \boldsymbol{\Lambda}_{vp}. \tag{51}$$

- viscoelastic conjugate state variable linearization:

$$\begin{aligned}\delta\boldsymbol{\sigma}^{vi} &= \frac{\partial\boldsymbol{\sigma}^{vi}}{\partial\boldsymbol{\sigma}} : \delta\boldsymbol{\sigma} + \frac{\partial\boldsymbol{\sigma}^{vi}}{\partial\boldsymbol{\epsilon}^{vi}} : \delta\boldsymbol{\epsilon}^{vi} + \frac{\partial\boldsymbol{\sigma}^{vi}}{\partial D}\delta D \\ &= \delta\boldsymbol{\sigma} - (1-D)\mathbb{C}^{vi} : \delta\boldsymbol{\epsilon}^{vi} + \mathbb{C}^{vi} : \boldsymbol{\epsilon}^{vi}\delta D \\ &= \boldsymbol{B}^p\delta r + \mathbb{B}^d : \delta\boldsymbol{\epsilon} - \mathbb{B}^d : \sum_{j=1}^{N_v}\delta\boldsymbol{\epsilon}^{vj} - (1-D)\mathbb{C}^{vi} : \delta\boldsymbol{\epsilon}^{vi} + \mathbb{C}^{vi} : \boldsymbol{\epsilon}^{vi}\Lambda_D\delta r \\ &= \mathbb{B}^d : \delta\boldsymbol{\epsilon} + \boldsymbol{B}^{wi}\delta r - \mathbb{B}^h : \delta\boldsymbol{\epsilon}^{vi} - \mathbb{B}^d : \sum_{j=1(j\neq i)}^{N_v}\delta\boldsymbol{\epsilon}^{vj} \end{aligned} \tag{52}$$

  with

$$\boldsymbol{B}^{wi} = \boldsymbol{B}^p + \mathbb{C}^{vi} : \boldsymbol{\epsilon}^{vi}\Lambda_D \tag{53}$$

$$\mathbb{B}^h = \mathbb{B}^d + (1-D)\mathbb{C}^{vi}. \tag{54}$$

- yield function linearization:

$$\begin{aligned}\delta f &= \frac{\partial f}{\partial \boldsymbol{\sigma}} : \delta\boldsymbol{\sigma} + \frac{\partial f}{\partial r}\delta r + \frac{\partial f}{\partial D}\delta D \\ &= f_\sigma : \delta\boldsymbol{\sigma} + f_r \delta r + f_D \delta D\end{aligned} \tag{55}$$

with

$$f_\sigma = \boldsymbol{\Lambda}_{vp} \ = \frac{\partial f}{\partial \boldsymbol{\sigma}} = \frac{\sqrt{3}\boldsymbol{\sigma}'}{2(1-D)\sqrt{J_2}} \tag{56}$$

$$f_r = \frac{\partial f}{\partial r} = H_p H_m r^{H_p - 1} \tag{57}$$

$$f_D = \frac{\partial f}{\partial D} = \frac{\sigma^{eq}}{(1-D)^2}. \tag{58}$$

Substituting equation (48) into equation (55) yields:

$$\begin{aligned}\delta f &= \boldsymbol{\Lambda}_{vp} : \left(\boldsymbol{B}^p \delta r + \mathbb{B}^d : \delta\boldsymbol{\epsilon} - \mathbb{B}^d : \sum_{j=1}^{N_v} \delta\boldsymbol{\epsilon}^{vj} \right) + f_r \delta r + f_D \Lambda_D \delta r \\ &= \boldsymbol{\Lambda}_{vp} : \left(\mathbb{B}^d : \delta\boldsymbol{\epsilon} - \mathbb{B}^d : \sum_{j=1}^{N_v} \delta\boldsymbol{\epsilon}^{vj} \right) + B^m \delta r\end{aligned} \tag{59}$$

where

$$B^m = \boldsymbol{\Lambda}_{vp} : \boldsymbol{B}^p + f_D \Lambda_D + f_r. \tag{60}$$

- viscoelastic criterion linearization:

$$\begin{aligned}\delta\boldsymbol{\phi}^{vi} &= \frac{\partial \boldsymbol{\phi}^{vi}}{\partial \boldsymbol{\sigma}^{vi}} : \delta\boldsymbol{\sigma}^{vi} + \frac{\partial \boldsymbol{\phi}^{vi}}{\partial \boldsymbol{\epsilon}^{vi}} : \delta\boldsymbol{\epsilon}^{vi} + \frac{\partial \boldsymbol{\phi}^{vi}}{\partial D}\delta D \\ &= \frac{1}{1-D}\left(\mathbb{V}^{vi}\right)^{-1} : \delta\boldsymbol{\sigma}^{vi} - \frac{1}{\Delta t}\delta\boldsymbol{\epsilon}^{vi} + \frac{1}{(1-D)^2}\left(\mathbb{V}^{vi}\right)^{-1} : \boldsymbol{\sigma}^{vi}\delta D.\end{aligned}$$

Substituting equation (52) into the above equation yields:

$$\delta\boldsymbol{\phi}^{vi} = \frac{1}{1-D}\left(\mathbb{V}^{vi}\right)^{-1} : \left(\mathbb{B}^{d} : \delta\boldsymbol{\epsilon} + \boldsymbol{B}^{wi}\delta r - \mathbb{B}^{h} : \delta\boldsymbol{\epsilon}^{vi} - \mathbb{B}^{d} : \sum_{j=1(j\neq i)}^{N_v} \delta\boldsymbol{\epsilon}^{vj} \right)$$

$$-\frac{1}{\Delta t}\delta\boldsymbol{\epsilon}^{vi} + \frac{1}{\left(1-D\right)^{2}}\left(\mathbb{V}^{vi}\right)^{-1} : \boldsymbol{\sigma}^{vi}\Lambda_{D}\delta r$$

$$= \frac{1}{1-D}\left(\mathbb{V}^{vi}\right)^{-1} : \left(\mathbb{B}^{d} : \delta\boldsymbol{\epsilon} - \mathbb{B}^{d} : \sum_{j=1(j\neq i)}^{N_v} \delta\boldsymbol{\epsilon}^{vj} \right) - \mathbb{B}^{vi} : \delta\boldsymbol{\epsilon}^{vi} - \boldsymbol{B}^{gi}\delta r \tag{61}$$

with

$$\mathbb{B}^{vi} = \frac{1}{1-D}\left(\mathbb{V}^{vi}\right)^{-1} : \mathbb{B}^{h} + \frac{1}{\Delta t}\mathbb{I} \tag{62}$$

$$\boldsymbol{B}^{gi} = -\frac{1}{1-D}\left(\mathbb{V}^{vi}\right)^{-1} : \boldsymbol{B}^{wi} - \frac{1}{\left(1-D\right)^{2}}\left(\mathbb{V}^{vi}\right)^{-1} : \boldsymbol{\sigma}^{vi}\Lambda_{D}. \tag{63}$$

- viscoplastic criterion linearization:

$$\delta\phi^{vp} = \frac{\partial\phi^{vp}}{\partial f}\delta f + \frac{\partial\phi^{vp}}{\partial r}\delta r$$

$$= \Omega^{*}\delta f - \frac{\delta r}{\Delta t} \tag{64}$$

with

$$\Omega^{*} = \frac{1}{P_{vp}}\left(\frac{f+|f|}{2R_{vp}}\right)^{P_{vp}^{-1}-1}\frac{1+sgn(f)}{2R_{vp}}. \tag{65}$$

Substituting equation (59) into equation (64) yields:

$$\delta\phi^{vp} = \Omega^{*}\left[\boldsymbol{\Lambda}_{vp} : \left(\mathbb{B}^{d} : \delta\boldsymbol{\epsilon} - \mathbb{B}^{d} : \sum_{j=1}^{N_v} \delta\boldsymbol{\epsilon}^{vj} \right) + \boldsymbol{B}^{m}\delta r\right] - \frac{\delta r}{\Delta t}. \tag{66}$$

Viscoelastic prediction-correction

In this algorithm, the total strain is considered constant ($\delta\boldsymbol{\epsilon} = 0$). Only the viscoelastic strains increments, $\delta\boldsymbol{\epsilon}^{vi}$, are activated and the remaining internal variables are assumed to be constant:

$$\delta r = \delta D = 0, \;\; \delta\boldsymbol{\epsilon}^{vp} = 0. \tag{67}$$

According to (35), the following tensorial equation is derived:

$$-\delta\boldsymbol{\phi}^{vi} = \boldsymbol{\phi}^{vi}. \tag{68}$$

Considering equation (67), the viscoelastic prediction-correction equation (68) is obtained as:

$$\mathbb{A}^{vi} : \sum_{j=1(j\neq i)}^{N_v} \delta\boldsymbol{\epsilon}^{vj} + \mathbb{B}^{vi} : \delta\boldsymbol{\epsilon}^{vi} = \boldsymbol{\phi}^{vi} \tag{69}$$

with

$$\mathbb{A}^{vi} = \frac{1}{1-D}\left(\mathbb{V}^{vi}\right)^{-1} : \mathbb{B}^{d} \tag{70}$$

where can be shown more clearly as:

$$\begin{bmatrix} \mathbb{B}^{v1} & \mathbb{A}^{v1} & \mathbb{A}^{v1} & . & . & . & \mathbb{A}^{v1} \\ \mathbb{A}^{v2} & \mathbb{B}^{v2} & \mathbb{A}^{v2} & . & . & . & \mathbb{A}^{v2} \\ \mathbb{A}^{v3} & \mathbb{A}^{v3} & \mathbb{B}^{v3} & . & . & . & \mathbb{A}^{v3} \\ . & . & . & . & . & . & . \\ . & . & . & . & . & . & . \\ . & . & . & . & . & . & . \\ \mathbb{A}^{vN_v} & \mathbb{A}^{vN_v} & \mathbb{A}^{vN_v} & . & . & . & \mathbb{B}^{vN_v} \end{bmatrix} \begin{bmatrix} \delta\boldsymbol{\epsilon}^{v1} \\ \delta\boldsymbol{\epsilon}^{v2} \\ \delta\boldsymbol{\epsilon}^{v3} \\ . \\ . \\ . \\ \delta\boldsymbol{\epsilon}^{vN_v} \end{bmatrix} = \begin{bmatrix} \boldsymbol{\phi}^{v1} \\ \boldsymbol{\phi}^{v2} \\ \boldsymbol{\phi}^{v3} \\ . \\ . \\ . \\ \boldsymbol{\phi}^{vN_v} \end{bmatrix}. \tag{71}$$

Full correction

Once $f \geq 0$, the viscoplastic deformation coupled with damage is activated (see section 'Full correction'). In order to implement the return mapping, full correction algorithm proposes an iterative algorithm where the damage and hardening state variable increments are also taken into account. However, the total strain is constant at each time step, and its increment $\delta\boldsymbol{\epsilon}$ is set to zero. According to (37), the iterative equations are derived as:

$$\begin{cases} -\delta\boldsymbol{\phi}^{vi} = \boldsymbol{\phi}^{vi}, \\ -\delta\phi^{vp} = \phi^{vp}, \end{cases} \tag{72}$$

where, using equations (66) and (70), it is expanded to:

$$\begin{cases} \mathbb{A}^{vi} : \sum_{j=1(j\neq i)}^{N_v} \delta\boldsymbol{\epsilon}^{vj} + \mathbb{B}^{vi} : \delta\boldsymbol{\epsilon}^{vi} + \boldsymbol{B}^{gi}\delta r = \boldsymbol{\phi}^{vi}, \\ \boldsymbol{A}^{vp} : \sum_{j=1}^{N_v} \delta\boldsymbol{\epsilon}^{vj} + B^{s}\delta r = \phi^{vp}, \end{cases} \tag{73}$$

where

$$\boldsymbol{A}^{vp} = \Omega^{*}\boldsymbol{\Lambda}_{vp} : \mathbb{B}^{d} \tag{74}$$

$$B^{s} = -\left(\Omega^{*}B^{m} - \frac{1}{\Delta t}\right). \tag{75}$$

Equation (73) is expanded to its tensorial form as:

$$\begin{bmatrix} \mathbb{B}^{v1} & \mathbb{A}^{v1} & \mathbb{A}^{v1} & . & . & . & \mathbb{A}^{v1} & \boldsymbol{B}^{g1} \\ \mathbb{A}^{v2} & \mathbb{B}^{v2} & \mathbb{A}^{v2} & . & . & . & \mathbb{A}^{v2} & \boldsymbol{B}^{g2} \\ \mathbb{A}^{v3} & \mathbb{A}^{v3} & \mathbb{B}^{v3} & . & . & . & \mathbb{A}^{v3} & \boldsymbol{B}^{g3} \\ . & . & . & . & . & . & . & . \\ . & . & . & . & . & . & . & . \\ . & . & . & . & . & . & . & . \\ \mathbb{A}^{vN_v} & \mathbb{A}^{vN_v} & \mathbb{A}^{vN_v} & . & . & . & \mathbb{B}^{vN_v} & \boldsymbol{B}^{gN_v} \\ \boldsymbol{A}^{vp} & \boldsymbol{A}^{vp} & \boldsymbol{A}^{vp} & . & . & . & \boldsymbol{A}^{vp} & B^{s} \end{bmatrix} \begin{bmatrix} \delta\boldsymbol{\epsilon}^{v1} \\ \delta\boldsymbol{\epsilon}^{v2} \\ \delta\boldsymbol{\epsilon}^{v3} \\ . \\ . \\ . \\ \delta\boldsymbol{\epsilon}^{vN_v} \\ \delta r \end{bmatrix} = \begin{bmatrix} \boldsymbol{\phi}^{v1} \\ \boldsymbol{\phi}^{v2} \\ \boldsymbol{\phi}^{v3} \\ . \\ . \\ . \\ \boldsymbol{\phi}^{vN_v} \\ \phi^{vp} \end{bmatrix}. \tag{76}$$

Tangent operators

The finite element solver not only requires defining the stress, but also it demands for updating tangent operators $\mathbb{T}^{\boldsymbol{\sigma}}_{\boldsymbol{\epsilon}}$, $\boldsymbol{T}^{\boldsymbol{\sigma}}_{\varphi^{nl}}$, $\boldsymbol{T}^{h}_{\boldsymbol{\epsilon}}$, and $T^{h}_{\varphi^{nl}}$ at each time step. As already indicated, solely $\mathbb{T}^{\boldsymbol{\sigma}}_{\boldsymbol{\epsilon}}$ and $\mathrm{T}^{\mathrm{h}}_{\varphi^{nl}}$ are required by UMAT and HETVAL. Before plastic flow activation, the tangent stiffness tensor, $\mathbb{T}^{\boldsymbol{\sigma}}_{\boldsymbol{\epsilon}}$, is defined as the viscoelastic tangent operator by ignoring Δr, and after exceeding the yield surface, the full tangent operator is requested, in which Δr is taken into account. In this sense, it is assumed that the nullity of the criteria is satisfied, then the criteria increments are derived as:

$$\Delta\boldsymbol{\phi}^{vi} = \frac{1}{1-D}\left(\mathbb{V}^{vi}\right)^{-1} : \Delta\boldsymbol{\sigma}^{vi} - \frac{1}{\Delta t}\Delta\boldsymbol{\epsilon}^{vi} + \frac{1}{(1-D)^{2}}\left(\mathbb{V}^{vi}\right)^{-1} : \boldsymbol{\sigma}^{vi}\Delta D = 0 \tag{77}$$

$$\Delta\phi^{vp} = \Omega^{*}\Delta f - \frac{\Delta r}{\Delta t} = \Omega^{*}\left(\boldsymbol{\Lambda}_{vp} : \Delta\boldsymbol{\sigma} + f_r\Delta r + f_D\Lambda_D\Delta r\right) - \frac{\Delta r}{\Delta t} = 0. \tag{78}$$

Substituting equations (52) and (48) into equations (77) and (78) respectively yields:

$$\Delta\boldsymbol{\phi}^{vi} = \mathbb{K}_{6(i)} : \Delta\boldsymbol{\epsilon} + \sum_{j=1}^{N_v} \mathbb{K}_{8(ij)} : \Delta\boldsymbol{\epsilon}^{vj} + \boldsymbol{K}_{7(i)}\Delta r = 0 \ , \tag{79}$$

$$\Delta\phi^{vp} \ = \boldsymbol{K}_9 : \Delta\boldsymbol{\epsilon} + \sum_{j=1}^{N_v} \boldsymbol{K}_{10} : \Delta\boldsymbol{\epsilon}^{vj} + K_{11}\Delta r = 0 \tag{80}$$

with

$$\mathbb{K}_{1(i)} = \frac{1}{1-D}\left(\mathbb{V}^{vi}\right)^{-1} \tag{81}$$

$$\mathbb{K}_{2(i)} = -\left(\mathbb{V}^{vi}\right)^{-1} : \mathbb{C}^{vi} - \frac{\mathbb{I}}{\Delta t} \tag{82}$$

$$\boldsymbol{K}_{3(i)} = \frac{1}{1-D}\left(\mathbb{V}^{vi}\right)^{-1} : \mathbb{C}^{vi} : \boldsymbol{\epsilon}^{vi}\Lambda_D + \frac{1}{(1-D)^2}\left(\mathbb{V}^{vi}\right)^{-1} : \boldsymbol{\sigma}^{vi}\Lambda_D \tag{83}$$

$$\boldsymbol{K}_4 = \Omega^* \boldsymbol{\Lambda}_{vp} \tag{84}$$

$$K_5 = \Omega^* f_r + \Omega^* f_D \Lambda_D - \frac{1}{\Delta t} \tag{85}$$

$$\mathbb{K}_{6(i)} = \mathbb{K}_{1(i)} : \mathbb{B}^d \tag{86}$$

$$\boldsymbol{K}_{7(i)} = \mathbb{K}_{1(i)} : \boldsymbol{B}^p \ + \boldsymbol{K}_{3(i)} \tag{87}$$

$$\sum_{j=1}^{N_v} \mathbb{K}_{8(ij)} : \Delta\boldsymbol{\epsilon}^{vj} = \mathbb{K}_{2(i)} : \Delta\boldsymbol{\epsilon}^{vi} - \mathbb{K}_{1(i)} : \mathbb{B}^d : \sum_{j=1}^{N_v} \Delta\boldsymbol{\epsilon}^{vj} \tag{88}$$

$$\boldsymbol{K}_9 = \boldsymbol{K}_4 : \mathbb{B}^d \tag{89}$$

$$\boldsymbol{K}_{10} = -\boldsymbol{K}_9 \tag{90}$$

$$K_{11} = \boldsymbol{K}_4 : \boldsymbol{B}^p + K_5. \tag{91}$$

Viscoelastic tangent operator. In order to derive the viscoelastic tangent modulus, Δr is ignored in equation (79), then $\Delta\boldsymbol{\epsilon}^{vi}$ with respect to $\Delta\boldsymbol{\epsilon}$ is given as:

$$\Delta\boldsymbol{\epsilon}^{vi} = \mathbb{K}_T^v : \Delta\boldsymbol{\epsilon} \tag{92}$$

with

$$\mathbb{K}_T^v = -\begin{bmatrix} \mathbb{K}_{8(11)} & \mathbb{K}_{8(12)} & \mathbb{K}_{8(13)} & \cdot & \cdot & \cdot & \mathbb{K}_{8(1N_v)} \\ \mathbb{K}_{8(21)} & \mathbb{K}_{8(22)} & \mathbb{K}_{8(23)} & \cdot & \cdot & \cdot & \mathbb{K}_{8(2N_v)} \\ \mathbb{K}_{8(31)} & \mathbb{K}_{8(32)} & \mathbb{K}_{8(33)} & \cdot & \cdot & \cdot & \mathbb{K}_{8(3N_v)} \\ \cdot & \cdot & \cdot & \cdot & \cdot & \cdot & \cdot \\ \cdot & \cdot & \cdot & \cdot & \cdot & \cdot & \cdot \\ \cdot & \cdot & \cdot & \cdot & \cdot & \cdot & \cdot \\ \mathbb{K}_{8(N_v1)} & \mathbb{K}_{8(N_v2)} & \mathbb{K}_{8(N_v3)} & \cdot & \cdot & \cdot & \mathbb{K}_{8(N_vN_v)} \end{bmatrix}^{-1} \begin{bmatrix} \mathbb{K}_{6(1)} \\ \mathbb{K}_{6(2)} \\ \mathbb{K}_{6(3)} \\ \cdot \\ \cdot \\ \cdot \\ \mathbb{K}_{6(N_v)} \end{bmatrix}. \tag{93}$$

The stress increment, $\Delta\boldsymbol{\sigma}$, without plastic deformation is given as:

$$\Delta\boldsymbol{\sigma} = (1-D)\mathbb{C}^e : \left(\Delta\boldsymbol{\epsilon} - \sum_{i=1}^{N_v} \Delta\boldsymbol{\epsilon}^{vi}\right). \tag{94}$$

Substituting equations (92) into (94) results in:

$$\Delta\boldsymbol{\sigma} = \underbrace{(1-D)\left(\mathbb{C}^e - \sum_{i=1}^{N_v} \mathbb{K}_T^v\right)}_{\mathbb{T}_\epsilon^\sigma} : \Delta\boldsymbol{\epsilon}. \tag{95}$$

Full tangent operator. Δr and $\Delta\boldsymbol{\epsilon}^{vi}$ with respect to $\Delta\boldsymbol{\epsilon}$ can be extracted from equations (79) and (80) as:

$$\begin{bmatrix} \Delta\boldsymbol{\epsilon}^{vi} \\ \Delta r \end{bmatrix} = \begin{bmatrix} \boldsymbol{X}^{vi} \\ \boldsymbol{X}^{r} \end{bmatrix} \Delta\boldsymbol{\epsilon} \tag{96}$$

where

$$\begin{bmatrix} \boldsymbol{X}^{v1} \\ \boldsymbol{X}^{v2} \\ \boldsymbol{X}^{v3} \\ \cdot \\ \cdot \\ \cdot \\ \boldsymbol{X}^{vN_v} \\ \boldsymbol{X}^{r} \end{bmatrix} = -\begin{bmatrix} \mathbb{K}_{8(11)} & \mathbb{K}_{8(12)} & \mathbb{K}_{8(13)} & \cdot & \cdot & \cdot & \mathbb{K}_{8(1N_v)} & \boldsymbol{K}_{7(1)} \\ \mathbb{K}_{8(21)} & \mathbb{K}_{8(22)} & \mathbb{K}_{8(23)} & \cdot & \cdot & \cdot & \mathbb{K}_{8(2N_v)} & \boldsymbol{K}_{7(2)} \\ \mathbb{K}_{8(31)} & \mathbb{K}_{8(32)} & \mathbb{K}_{8(33)} & \cdot & \cdot & \cdot & \mathbb{K}_{8(3N_v)} & \boldsymbol{K}_{7(3)} \\ \cdot & \cdot & \cdot & \cdot & \cdot & \cdot & \cdot & \cdot \\ \cdot & \cdot & \cdot & \cdot & \cdot & \cdot & \cdot & \cdot \\ \cdot & \cdot & \cdot & \cdot & \cdot & \cdot & \cdot & \cdot \\ \mathbb{K}_{8(N_v1)} & \mathbb{K}_{8(N_v2)} & \mathbb{K}_{8(N_v3)} & \cdot & \cdot & \cdot & \mathbb{K}_{8(N_vN_v)} & \boldsymbol{K}_{7(N_v)} \\ \boldsymbol{K}_{10} & \boldsymbol{K}_{10} & \boldsymbol{K}_{10} & \cdot & \cdot & \cdot & \boldsymbol{K}_{10} & K_{11} \end{bmatrix}^{-1} \begin{bmatrix} \mathbb{K}_{6(1)} \\ \mathbb{K}_{6(2)} \\ \mathbb{K}_{6(3)} \\ \cdot \\ \cdot \\ \cdot \\ \mathbb{K}_{6(N_v)} \\ \boldsymbol{K}_9 \end{bmatrix} \tag{97}$$

Substituting equation (96) into equation (48) yields:

$$\Delta\boldsymbol{\sigma} = \underbrace{\left(\boldsymbol{B}^p \otimes \boldsymbol{X}^r + \mathbb{B}^d - \mathbb{B}^d : \sum_{j=1}^{N_v} \boldsymbol{X}^{vj}\right)}_{\mathbb{T}_\epsilon^\sigma} : \Delta\boldsymbol{\epsilon} \ . \tag{98}$$